

Large-eddy simulation of gusty wind turbulence over a travelling wave

Xuanting Hao¹ and Lian Shen^{1,†}

¹Department of Mechanical Engineering and St. Anthony Falls Laboratory, University of Minnesota, Minneapolis, MN 55455, USA

(Received 6 January 2022; revised 30 May 2022; accepted 23 June 2022)

Wind gustiness in the marine atmospheric boundary layer affects significantly the dynamics of air–sea interaction. To understand the impacts of wind gust events, we perform large-eddy simulation of wind turbulence over a travelling wave to investigate the response of the wind field to an impulsive wind speed increase or decrease. It is found that the turbulence fluctuations and the terms in the turbulent kinetic energy budget equation have a delayed response to the change in the mean flow, while the response of the wave-coherent motions is quasi-stationary. The wave-coherent motions are investigated quantitatively through comparison with a viscous curvilinear model developed by Cao *et al.* (*J. Fluid Mech.*, vol. 901, 2020, A27) and Cao & Shen (*J. Fluid Mech.*, vol. 919, 2021, A38). We observe an asymmetric hysteresis between the growing wind and the decaying wind in the evolution of the form drag and the viscous drag. We find further that the variation of the wave growth rate during the wind gust is related closely to the contribution from the out-of-phase component of the vertical velocity. Our discoveries provide evidence for the necessity of improving non-equilibrium turbulence and wind input modelling to account for the wind gustiness effect in future studies.

Key words: air/sea interactions, atmospheric flows, turbulent boundary layers

1. Introduction

Wind gustiness is a ubiquitous phenomenon in the atmospheric boundary layer. When the gustiness is strong, the variation in the wind speed becomes comparable to the average value, which has significant effects on air–sea interactions. In weather and climate models, the wind gustiness parametrization is important because computations based on the average wind speed can underestimate the air–sea fluxes significantly, especially when

† Email address for correspondence: shen@umn.edu

the mean wind speed is low (Zeng *et al.* 2002). Additionally, the wind gustiness may affect the upper ocean temperature (Giglio *et al.* 2017) and the fluctuations in the electricity power output generated by wind turbines (Stevens & Meneveau 2017).

For the interaction between wind and waves, the gustiness effect is often found to be non-negligible. In a laboratory experiment, Waseda, Toba & Tulin (2001) investigated wave evolution in a water tank by imposing a sudden change in wind speed. They identified the deviation from the 3/2 power law (Toba 1972) that indicates a local wind–wave equilibrium state, i.e. $H_s \propto (gu_*)^{1/2} T_s^{3/2}$, where H_s is the significant wave height, u_* is the air friction velocity and T_s is the significant wave period. Their results also showed hysteresis in the wave height responses to increasing and decreasing wind. Abdalla & Cavaleri (2002) used a random sequence to model the wind speed fluctuations, which was incorporated into the wind input source term in an operational phase-averaged wave model (Komen *et al.* 1994). Abdalla & Cavaleri (2002) then performed a series of simulations, including idealized runs based on prescribed physical conditions, and practical runs based on historical data from meteorological observations. Their results showed that the gustiness effects on slow waves are limited, while for fast waves, a gusty wind field can enhance significantly the wave growth compared with that under constant winds. Annenkov & Shrira (2011) investigated numerically the evolution of a nonlinear wave field, and found that the integral wave properties under a gusty wind forcing are consistent with those under an effective constant wind forcing. It should be noted that the sources of the gustiness used in the above two modelling-based studies are different. Abdalla & Cavaleri (2002) considered the variations in the observable wind speed. Annenkov & Shrira (2011) modelled the gustiness by adjusting the wave energy growth rate, which is challenging, generally, to measure directly from observations. In a field study, Hwang, García Nava & Ocampo-Torres (2011) observed that the wave energy growth in unsteady wind forcing is quantitatively different from that in a steady forcing. Their results also provide evidence of the hysteresis effect of wave development, namely, a much slower rate of change of the characteristic wave properties in decaying wind speed than in the growing wind. More recently, Zavatsky & Shemer (2017) performed a laboratory experiment to investigate the initial wave generation from a quiescent surface under impulsive wind forcing. Model development for gustiness effect is still at an early stage. In the European Centre for Medium-range Weather Forecasts (ECMWF) model (ECMWF 2020), the gustiness impact is parametrized through a simple model mainly to enhance the wind energy input to waves.

While the past several decades saw a growing number of studies on wind–wave interaction, most of the theoretical and numerical studies assumed that the wind turbulence is statistically stationary. In the quasi-laminar model proposed by Miles (1957), the wind field is simplified as the superposition of a prescribed mean profile and wave-induced resonant motions, while the effects of turbulence and viscosity are neglected. The critical layer was found to play a dominant role in wave growth, which has been substantiated by field observations (Hristov, Miller & Friehe 2003). Belcher & Hunt (1993) considered the turbulence impact on the wave growth through the non-separated sheltering mechanism, which was found to be important for slow waves. Nikolayeva & Tsimring (1986) and Miles & Ierley (1998) considered the effect of wind gustiness in the study of wave growth. But in both studies, the mean wind velocity profiles were assumed to be slowly varying in time, and the transient dynamics were neglected in the equivalent steady flow. In canonical numerical configurations (e.g. Sullivan, McWilliams & Moeng 2000), the wind turbulence field is simulated over a monochromatic travelling wave, and this framework has been used widely to explore the steady-state features of turbulent flows in wind–wave interactions.

For example, Kihara *et al.* (2007) studied the dependence of wave-coherent motions on the wave age. Yang & Shen (2010) showed a significant impact of wave on the near-surface coherent vortical structures. Based on the transformed Navier–Stokes equations on a boundary-fitted grid, Hara & Sullivan (2015) derived a momentum balance equation and elucidated the role of the wave-induced stresses. Recently, Åkervik & Vartdal (2019) proposed an approach to split the wind field into a shear flow and a wave-induced part. The linear solution obtained using this method was found to capture the main features of the flow in the cases with high wave ages, but large deviations were observed at low wave ages. They also found that the nonlinear solution, which takes account of turbulence forcing, is in close agreement with the large-eddy simulation (LES) results in both cases. Cao, Deng & Shen (2020) developed a viscous curvilinear model to predict the wave-coherent motions based on the mean wind velocity profile and the wave orbital velocity. The model shows excellent performance when applied to wind over opposing waves and wind over fast following waves, while for wind over slow following waves, notable discrepancies between the model prediction and the simulation results were observed (Cao *et al.* 2020; Cao & Shen 2021). Husain, Hara & Sullivan (2022*a,b*) performed numerical experiments of wind turbulence when the waves are travelling at an oblique angle to the wind direction, and they identified a strong impact of the oblique angles on the air–sea momentum flux. In the studies reviewed above, the wind field is typically driven by a constant pressure gradient in the domain or a constant velocity or shear stress at the domain top, and the resulting turbulence statistics are stationary in time. Therefore, the wind–wave energy transfer is determined by the steady-state variables, such as the characteristic wind speed and the characteristic wave properties.

Some recent simulation-based studies have also investigated more complex physical processes by taking into account the spatial/temporal heterogeneity in the wind–wave system. For example, Yang, Deng & Shen (2018) studied the wind turbulence over breaking waves, and elucidated the transient and non-equilibrium features of the turbulence locally in space and time. Irregular broadband wave fields have also been used in the problem set-up of several studies (Sullivan, McWilliams & Patton 2014; Wang *et al.* 2020), although the temporal variation of the mean profile was not considered. Dynamically coupled wind–wave evolution was studied recently by Hao & Shen (2019). In that study, the pressure gradient used to drive the wind field was constant, and because the characteristic time scale of the nonlinear wave evolution was considerably larger than the wave periods, the wind turbulence field was largely statistically stationary in time. In experimental studies, it is also common practice to maintain a certain wind speed (e.g. Liberzon & Shemer 2011; Grare *et al.* 2013; Yousefi, Veron & Buckley 2020). While spatial heterogeneity may appear in the water tank because of wave evolution downstream (Zavatsky & Shemer 2012) and airflow separation (Buckley, Veron & Yousefi 2020), the wind turbulence field is statistically stationary.

In summary of the reviews above, our knowledge on the non-stationary turbulence features in wind–wave interaction subject to wind gustiness is rather limited. In the present study, we investigate the response of an initially steady wind field above a prescribed wave to a growing/decaying wind gust event. Our objective is to elucidate the key airflow transient processes, including the evolution of turbulence and wave-coherent motions. We also study the change in the wind–wave energy transfer associated with the gust, and explore the underlying mechanisms. To achieve this goal, we perform LES of the wind turbulence on a wave-boundary-fitted grid, a numerical framework that has been validated in various studies (e.g. Yang & Shen 2011*a,b*; Hao & Shen 2019; Cao *et al.* 2020). We do

not consider the wave evolution during the wind gust because the time scale of the wind gust is only a few wave periods, and it has been shown that the time scale for the wave to have noticeable change is much larger (Annenkov & Shrira 2011). The remainder of this paper is organized as follows. In § 2, we introduce the simulation configuration and the case design. In § 3, we present results on the overall wind field evolution (§ 3.1), the transient features of the turbulent stresses (§ 3.2), the wave-coherent motions (§§ 3.3 and 3.4) and the wave growth rate (§ 3.5). Finally, conclusions are given in § 4.

2. Methodology and problem set-up

2.1. Large-eddy simulation on a boundary-fitted grid

Following our previous work (Hao & Shen 2019), the wind turbulence is simulated using wall-resolved LES. The governing equations for the air motions are written as

$$\frac{\partial u_i}{\partial x_i} = 0, \tag{2.1}$$

$$\frac{\partial u_i}{\partial t} + u_j \frac{\partial u_i}{\partial x_j} = -\frac{1}{\rho} \frac{\partial p}{\partial x_i} - \frac{\partial \tau_{ij}^d}{\partial x_j} + \nu \frac{\partial^2 u_i}{\partial x_j \partial x_j} + B(t) \delta_{i1}, \tag{2.2}$$

where $u_i (i = 1, 2, 3) = (u, v, w)$ denotes the filtered velocity in LES, p is the filtered modified pressure, τ_{ij}^d is the trace-free part of the subgrid-scale (SGS) stress tensor, ρ is the air density, ν is the kinematic viscosity of air, $B(t)$ denotes the driving force used for the flow rate control, and x, y and z denote the streamwise, spanwise and vertical coordinates, respectively. The domain sizes are denoted by L_x, L_y and L_z . The schematic of the computational domain is shown in figure 1(a).

To account for the geometric deformation caused by the wave profile, the LES governing equations are solved on a wave surface boundary-fitted grid via a transformation from the physical space (x, y, z, t) to the computational space (ξ, ψ, ζ, τ) . The details of the grid transformation and the numerical solver are provided in Appendix A. Here we give an overview of the numerical scheme. Details can be found in Yang & Shen (2011a,b). At each time step, the spatial derivatives in the horizontal directions are calculated using Fourier transforms, and those in the vertical direction are calculated using second-order finite differences. The SGS stress tensor is calculated using the dynamic Smagorinsky model (Smagorinsky 1963; Germano *et al.* 1991; Lilly 1992). The momentum equation is first advanced in time without the pressure term to obtain the interim velocity field. The Poisson equation for the pressure is then solved, and the pressure field is used to correct the velocity field to satisfy the continuity equation. The second-order Adam–Bashforth scheme is used for time advancement. The simulation starts from randomly generated turbulent motions imposed on a logarithmic mean velocity profile, with a flat bottom boundary initially to expedite the simulation process. The wave kinematics are then incorporated into the boundary condition through a relaxation process. More details and validations of the numerical solver can be found in Yang & Shen (2011a,b), Cao *et al.* (2020) and Cao & Shen (2021).

In previous studies on the steady state wind–wave interaction, the wind turbulence is driven by a constant pressure gradient (e.g. Yang, Meneveau & Shen 2013; Åkervik & Vartdal 2019; Wang *et al.* 2020), or by a constant velocity or shear stress at the top boundary of the computational domain (Sullivan *et al.* 2000; Druzhinin, Troitskaya & Zilitinkevich 2012; Cao *et al.* 2020; Cao & Shen 2021) to maintain a constant flow rate. To model the wind gust event, we apply a time-varying pressure gradient $\rho B(t)$ to control

Gusty wind turbulence over a travelling wave

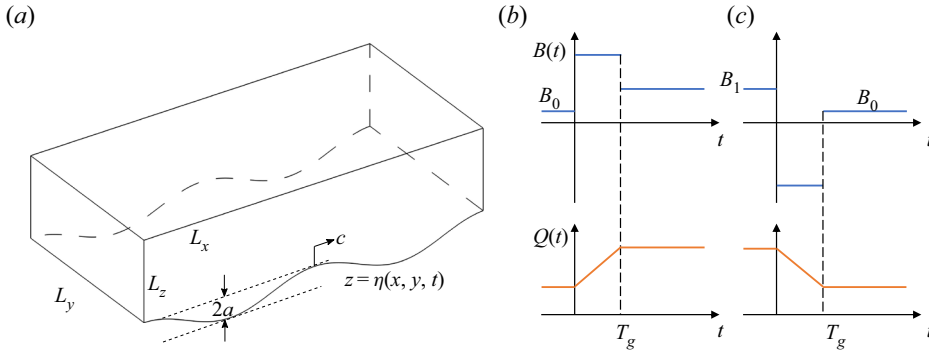


Figure 1. Sketch of (a) the computational domain, and the flow rate $Q(t)$ response to the driving force $B(t)$ in (b) the growing wind and (c) the decaying wind.

the flow rate of the wind field. In the first stage of the simulation, this driving force is set to guarantee a constant flow rate, which then varies linearly in a short time duration $0 < t < T_g$. The expression for $B(t)$ is

$$B(t) = \frac{dQ}{dt} \frac{1}{hL_y} - \frac{\tau_v(t) + \tau_p(t)}{\rho h}, \quad (2.3)$$

where $h = L_z$ is the vertical domain size, dQ/dt is the desired rate of change of the volumetric flow rate Q , $\tau_v(t)$ is the total viscous drag at the top boundary and the wave surface, and $\tau_p(t)$ is the form drag at the wave surface. Generally, the second term is not a constant because $\tau_v(t)$ and $\tau_p(t)$ vary in time. However, its contribution to $B(t)$ is negligibly small compared with the first term in typical gust events. After the flow rate has reached the designed value, the force is assigned a different value to maintain the flow. For a growing wind, dQ/dt is positive (figure 1b), while for a decaying wind, dQ/dt is negative (figure 1c). The flow rate control scheme used here is similar to that in computational studies of transient turbulent channel flows (e.g. He & Seddighi 2015), and is a close approximation to the wind speed control in laboratory studies (Waseda *et al.* 2001; Zavadsky & Shemer 2017).

The simulation parameters are summarized in table 1. To facilitate the decomposition of the turbulence field, we adopt the canonical set-up of wind over a prescribed monochromatic progressive wave. The wave steepness in our simulation is set to a typical value $ak = 0.05$, where a is the wave amplitude, and k is the wavenumber. A wide range of wave ages is selected for the initial wind–wave state, including both slow waves (e.g. $c/u_* = 4.4$ in case CU8) at the early stage of wind–wave generation (Belcher & Hunt 1993; Janssen 2004), and fast waves (e.g. $c/u_* = 41.6$ in case CU42) that are typically found under swell-dominated sea conditions (Sullivan *et al.* 2008). Following previous wind–wave studies (Henn & Sykes 1999; Calhoun, Street & Koseff 2001; Yang *et al.* 2013), we use a computational domain $(L_x, L_y, L_z) = (2\lambda, \lambda, \lambda)$, where λ is the wavelength. The domain size in the streamwise direction enables the simulation of turbulence coherent motions larger than λ , and is sufficiently large to produce the correct temporal correlation in the turbulence statistics (Hao, Cao & Shen 2021). The grid number is $N_x \times N_y \times N_z = 128 \times 256 \times 96$. To capture accurately the turbulent motions of the smallest eddies in the simulation, we choose the appropriate initial and final Reynolds numbers such that the grid resolutions satisfy the criterion of wall-resolved LES (Choi & Moin 2012). Note that the final Reynolds number in table 1 corresponds to the

Case	Gust event	$c^+ = c/u_*$	$Re_\tau = u_*\lambda/\nu$	$(\Delta\xi^+, \Delta\psi^+, \Delta\xi_{min}^+)$
CU8	Growing	8.3 → 4.4	2000 → 3805	(46.9, 11.7, 0.32) → (89.2, 22.3, 0.61)
	Decaying	4.4 → 8.3	3805 → 2000	(89.2, 22.3, 0.61) → (46.9, 11.7, 0.32)
CU19	Growing	19.3 → 10.2	2000 → 3805	(46.9, 11.7, 0.32) → (89.2, 22.3, 0.61)
	Decaying	10.2 → 19.3	3805 → 2000	(89.2, 22.3, 0.61) → (46.9, 11.7, 0.32)
CU42	Growing	41.6 → 21.9	2000 → 3805	(46.9, 11.7, 0.32) → (89.2, 22.3, 0.61)
	Decaying	21.9 → 41.6	3805 → 2000	(89.2, 22.3, 0.61) → (46.9, 11.7, 0.32)

Table 1. Numerical parameters of the simulations. Here, c^+ is the ratio of the wave phase velocity to the instantaneous friction velocity u_* , also known as the wave age, Re_τ is the Reynolds number based on the friction velocity and the wavelength λ , (N_x, N_y, N_z) are the grid numbers, and $(\Delta\xi^+, \Delta\psi^+, \Delta\xi_{min}^+)$ are the sizes of the first grid above the wave surface, normalized in wall units. Note that $\Delta\xi^+$ and $\Delta\psi^+$ are the effective values after accounting for de-aliasing in the Fourier spectral method.

Case	Gust event	T_g/T	u_*T_g/h
CU8	Growing	0.44	0.053 → 0.10
	Decaying	0.44	0.10 → 0.053
CU19	Growing	1.0	0.053 → 0.10
	Decaying	1.0	0.10 → 0.053
CU42	Growing	2.2	0.053 → 0.10
	Decaying	2.2	0.10 → 0.053

Table 2. Time duration of the wind gust event T_g , normalized by the wave period T and the largest eddy turnover time h/u_* .

new equilibrium state of the wind turbulence after the simulations are performed for a sufficiently long time after the wind gust ends. The simulations are performed in the fixed frame of reference, and in the following analysis related to wave-coherent motions, a frame translating with velocity $(c, 0, 0)$ is considered.

The time scales of the wind gust are summarized in table 2. The wind gust duration T_g is a few wave periods. Since there is no rigorous definition of a wind gust duration, T_g is assumed equivalent to a dimensional time scale of $O(1 - 10)$ s and therefore agrees with the 20 s limit adopted by the U.S. National Weather Service and the 3 s standard recommended by World Meteorological Organization (WMO) (2018). According to the wave tank experiment of Waseda *et al.* (2001), the initial adjustment time of slow waves ($c/u_* = 1 - 1.5$) responding to the wind gust event is $15T - 20T$. They also showed that for a field case ($c/u_* = 9$), this time scale becomes $210T - 420T$. In the following analysis, we focus on a short period during and after the wind gust event. Therefore, the changes in the wave properties can be neglected.

For each case shown in table 1, the growing and decaying wind gust events are simulated separately. We first perform the simulation at the initial Reynolds number, and after a statistically stationary state is reached, we impose a gust event on the steady wind turbulence field by varying the driving force $B(t)$ as described in (2.3) and shown in figure 1(b). Because of the rapid gust event, the wind turbulence field is non-stationary and no longer ergodic. It is therefore inappropriate to approximate the Reynolds averaging with the time averaging during this period. To address this issue, we perform 50 ensemble runs for each simulation, so that the turbulence statistics can be calculated but with a substantially increased computational cost. Note that for the above reason, some statistical

results are less smooth compared to the steady setting where time averaging can be performed, but this does not affect the conclusions of the analyses.

2.2. Triple decomposition and normalization

In the following analyses, the turbulence field is decomposed into three parts (Hussain & Reynolds 1972):

$$u = \langle u \rangle + u' = U + \tilde{u} + u', \tag{2.4}$$

where U denotes the mean profile, \tilde{u} denotes the wave-coherent motions, and u' is the ‘pure’ turbulent motion. The operator $\langle \cdot \rangle$ is defined by the phase average of all ensemble simulations,

$$\langle u \rangle(\xi, \zeta, t) = \frac{1}{NN_y} \sum_{n,j} u_n(\xi - ct, y_j, \zeta, t), \tag{2.5}$$

where u_n is the instantaneous quantity in the n th simulation ($n = 1, \dots, N; N = 50$). The phase-shift operation can be calculated conveniently via Fourier transform.

At each constant ζ , a wave-coherent component (take \tilde{u} as an example) can be written as

$$\tilde{u}(x, t) = \text{Re}[\tilde{u}](t) \cos(kx) - \text{Im}[\tilde{u}](t) \sin(kx), \tag{2.6}$$

where $\text{Re}[\tilde{u}]$ and $\text{Im}[\tilde{u}]$ are the real and imaginary parts of the Fourier coefficient, respectively. Traditionally, $\text{Re}[\tilde{u}] \cos(kx)$ and $\text{Im}[\tilde{u}] \sin(kx)$ are also called the in-phase and out-of-phase components, respectively (e.g. Belcher & Hunt 1993). An alternative form is $\tilde{u}(x, t) = |\tilde{u}| \cos(kx + \phi_{\tilde{u}})$, where $|\tilde{u}| = (\text{Re}[\tilde{u}]^2 + \text{Im}[\tilde{u}]^2)^{1/2}$ and $\phi_{\tilde{u}} = \tan^{-1}(\text{Im}[\tilde{u}]/\text{Re}[\tilde{u}])$ are the amplitude and phase of \tilde{u} , respectively. With respect to the wave profile, the real (imaginary) part, i.e. the in-phase (out-of-phase) component, corresponds to the symmetry (anti-symmetry) on the two sides of the wave crest.

Because of the gust events, the near-wall turbulence states, including the wall stress and the friction velocity, are non-stationary. In the following analyses, we use two types of scaling for normalization. Quantities with the superscript ‘+’ are normalized in the instantaneous time-variant wall units. In the second type of scaling, we introduce the superscripts ‘+0’ to denote the time-invariant normalization under the initial turbulent flow condition in the growing wind, and the corresponding friction velocity is denoted by $u_{*,0}$.

3. Results

3.1. Overview of wind turbulence field evolution

In this section, we first give an overview of the wind field evolution with a focus on the turbulent motion (u', v', w') defined in (2.4). For the length consideration of the paper, we present results in the growing wind of case CU8 when the flow dynamics are similar among the different cases in table 1. Figure 2 shows u' and w' at the start and end of the growing wind gust. The magnitude of u' is generally stronger than w' at both $t = 0$ and $t = T_g$, as shown by their contours on the x - z and y - z planes. The streaks near the wave surface, denoted by the isosurfaces of u' , are enhanced significantly after the impact of the wind gust. On the other hand, the isosurfaces of w' at $t = 0$ and $t = T_g$ are qualitatively similar. Explanations for these differences are provided from the analyses in § 3.2.

The mean wind profiles before, during and shortly after the gust event are plotted in figure 3. During the gust event $0 < t/T_g < 1$, the mean flow away from the wave

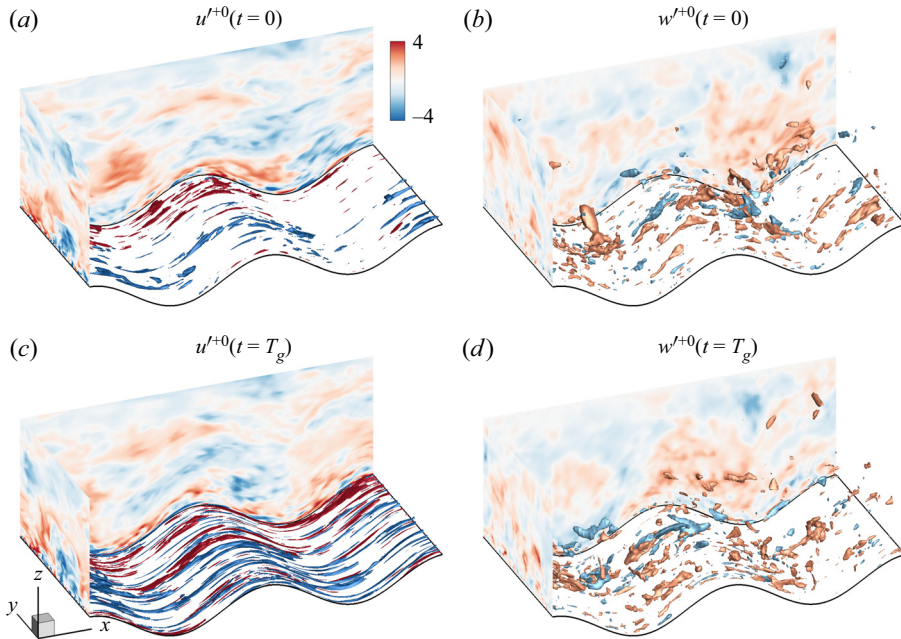


Figure 2. Turbulent motions at (a,b) $t = 0$ and (c,d) $t = T_g$ for the growing wind in case CU8. Plotted are the contours of u' and w' on the x - z and y - z planes, and the isosurfaces corresponding to $u'^{+0} = \pm 7$ in (a,b) and $w'^{+0} = \pm 3$ in (c,d), where the superscript '+0' denotes the normalization based on the wall unit at the initial state (see table 1).

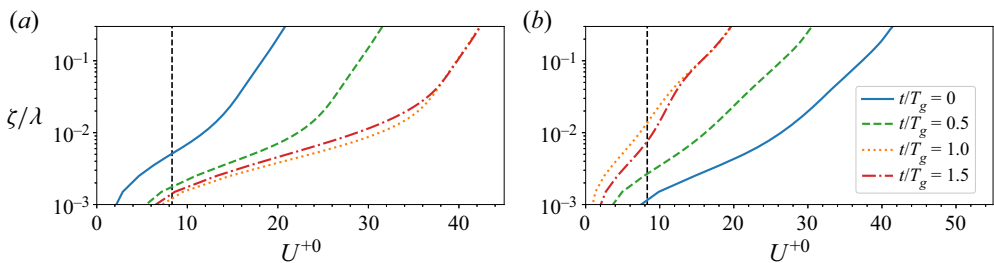


Figure 3. Evolution of the mean wind velocity profiles in (a) the growing wind and (b) the decaying wind, in case CU8. The profiles are normalized in the initial wall unit and plotted during $0 \leq t/T_g \leq 1.5$. The black dashed line denotes $U = c$.

surface ($\zeta > 0.01\lambda$) experiences a similar change and the velocity profiles are shifted by a roughly constant value. The dominant mechanism can be understood through the averaged streamwise momentum equation, which reduces to $\partial U/\partial t = B(t)$ to the leading order. Since $B(t)$ is nearly a constant, the time variation in the mean profile is linear and uniform. While a logarithmic region remains in the mean profile at the end of the gust $t = T_g$, the wind turbulence is in a non-equilibrium state. Therefore, the slope of the mean profile is no longer determined only by the friction velocity, and the mean profile cannot be used to calculate the wave growth rate in the same way as when the wind turbulence is steady (Miles 1957; Belcher & Hunt 1993) or quasi-stationary (Miles & Ierley 1998). In the region near the wave surface $\zeta < 0.01\lambda$, the velocity gradient (i.e. the mean shear) changes significantly during the gust because of the boundary condition constraint imposed by the

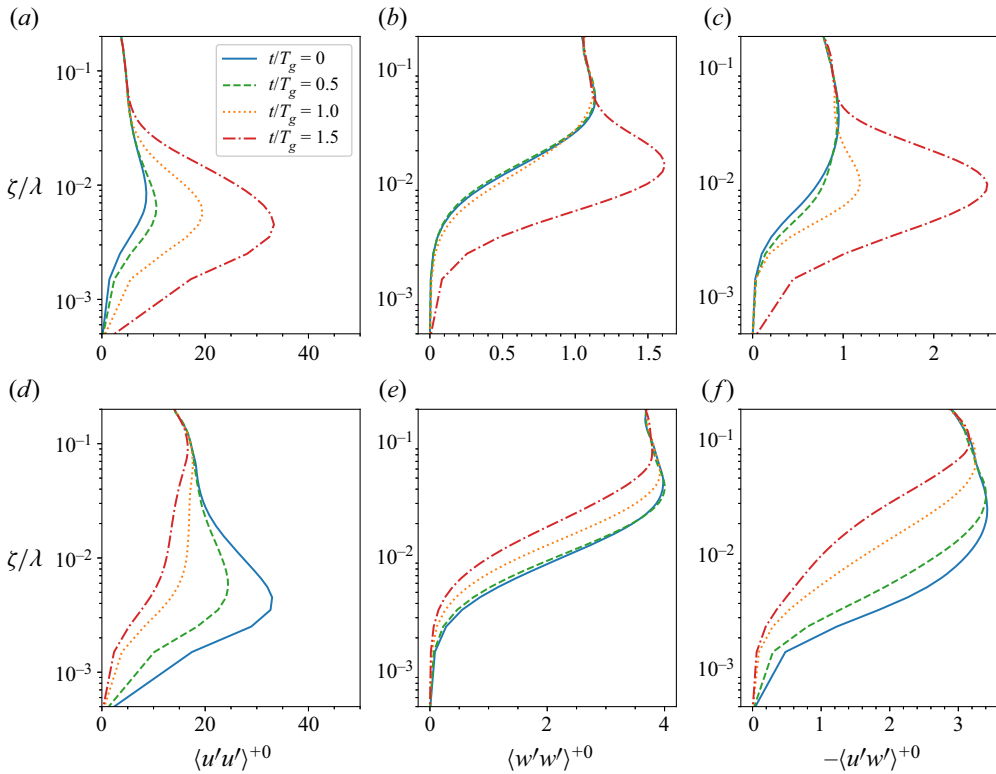


Figure 4. Vertical distribution of the Reynolds stresses for (a–c) the growing wind and (d–f) the decaying wind, in case CU8.

wave surface (see Appendix B). After the gust event, the wind field continues to evolve (comparing the profiles at $t = T_g$ and $t = 1.5T_g$ in figure 3) and a new equilibrium state can be established after a sufficiently long time. Compared with the wind gust event, the temporal variations in the wind field after $O(2T_g - 4T_g)$ are less drastic in the return to equilibrium and therefore excluded from the following analysis.

The response of turbulence to the wind gust is in sharp contrast to that of the mean velocity profile. Figure 4 shows the profiles of Reynolds stress components at several time instants during and after the wind gust event in case CU8. Here, $\langle v'v' \rangle$ is not plotted because its evolution is qualitatively similar to $\langle w'w' \rangle$. When the growing wind gust occurs ($0 < t < T_g$), we observe a rapid increase in the streamwise velocity fluctuations $\langle u'u' \rangle$ (figure 4a), while $\langle w'w' \rangle$ (figure 4b) has relatively stable values, and the evolution speed of $\langle u'w' \rangle$ (figure 4c) is between those of $\langle u'u' \rangle$ and $\langle w'w' \rangle$. At $t = 1.5T_g$, the magnitudes of all these Reynolds stress components become significantly larger as the turbulence field continues to evolve. In the decaying wind (figure 4d–f), the responses of the turbulent stress first appear near the wave surface and then extend to the outer region. These results are similar to the pipe flow experiment of accelerating and decelerating turbulence (He & Jackson 2000). The behaviours of the turbulent stresses are related closely to the gust-induced change in the mean shear. As shown above, the mean velocity profile exhibits a linear and uniform time variation such that the mean shear remains constant in the outer region and changes drastically only near the wave surface.

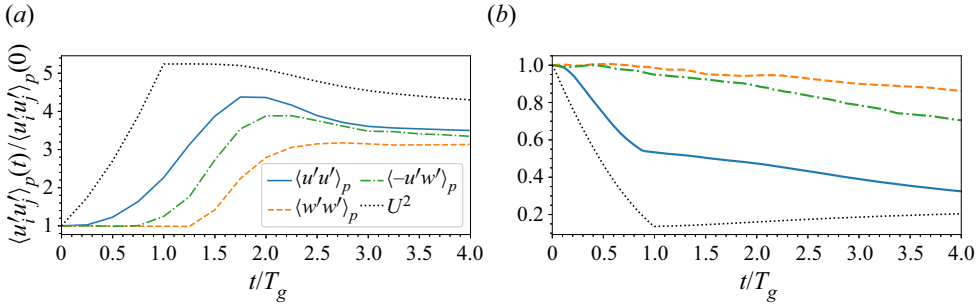


Figure 5. Time variation of the peak values of the turbulence variances in (a) the growing wind and (b) the decaying wind, in case CU8. Also plotted is the mean flow energy $U^2(t)$ at $\zeta = 0.051\lambda$. All terms are normalized by their values at $t = 0$.

The evolution of the Reynolds stresses is also demonstrated by tracking their peak values in time, shown in figure 5. Here, we also plot the time variation of the mean flow energy $U^2(t)/U^2(0)$ in the region $\zeta > 0.01\lambda$. As expected, the mean flow sees a real-time response with the onset of the gust. The peak streamwise turbulence variation $\langle u'u' \rangle_p = \max \langle u'u' \rangle$ changes rapidly after a short delay. When the wind is growing, an overshoot appears in $\langle u'u' \rangle_p$ after the gust ends, and its temporal evolution is qualitatively similar to the channel flow result (He & Seddighi 2015). The other two components, $\langle w'w' \rangle_p$ and $\langle -u'w' \rangle_p$, experience relatively less change in the growing and decaying wind gust. Compared with the evolution of the mean flow energy, the turbulence peak values show a delayed response (also known as the memory effect) to the gust. Because of this phase delay, the turbulent kinetic energy (TKE) relative to the mean energy, i.e. $\langle u'_i u'_i \rangle / U^2$, decreases in the growing wind and increases in the decaying wind. Detailed explanations are provided by the turbulence budget analysis in the next subsection.

3.2. Transient behaviours of a Reynolds stress budget and wave-induced effect

We perform a Reynolds stress budget analysis in this subsection to investigate the mechanism responsible for the turbulent stress evolution shown in § 3.1. In a previous study by Yang & Shen (2010), the budget of the TKE under the steady wind–wave condition was obtained. The detailed budget for the Reynolds stress components in unsteady wind fields over waves, however, was rarely reported. Following the work of Xuan, Deng & Shen (2020) on Langmuir turbulence under waves, we can write the Reynolds stress budget equation of wind turbulence in the frame of reference moving with the wave as

$$\frac{\partial \langle u'_i u'_j \rangle}{\partial t} = \underbrace{-(U - c) \cdot \nabla \langle u'_i u'_j \rangle}_A + \underbrace{\nu \nabla^2 \langle u'_i u'_j \rangle}_{D^v} - \underbrace{\langle u'_i u'_k \rangle \frac{\partial U_j}{\partial x_k} - \langle u'_j u'_k \rangle \frac{\partial U_i}{\partial x_k}}_{P^m} - \underbrace{\langle u'_i u'_k \rangle \frac{\partial \tilde{u}_j}{\partial x_k} - \langle u'_j u'_k \rangle \frac{\partial \tilde{u}_i}{\partial x_k}}_{P^w}$$

Gusty wind turbulence over a travelling wave

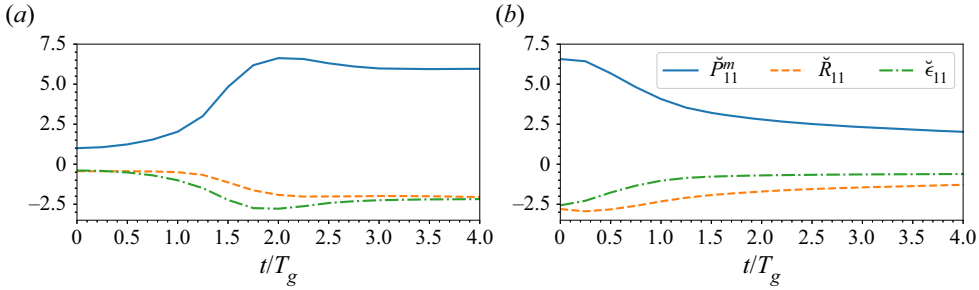


Figure 6. Time variation of the integrated budget terms for $\langle u'u' \rangle$ for (a) the growing wind and (b) the decaying wind in case CU8. All terms are normalized by $\check{P}_{11}^m(t = 0)$.

$$\begin{aligned}
 & \underbrace{-\frac{1}{\rho} \left(\frac{\partial \langle p'u'_i \rangle}{\partial x_j} + \frac{\partial \langle p'u'_j \rangle}{\partial x_i} \right)}_{T^p} + \underbrace{\left\langle \frac{p'}{\rho} \left(\frac{\partial u'_i}{\partial x_j} + \frac{\partial u'_j}{\partial x_i} \right) \right\rangle}_R \\
 & \underbrace{-\frac{\partial \langle u'_i u'_j u'_k \rangle}{\partial x_k} - \frac{\partial \langle u'_i \tau'_{jk} \rangle}{\partial x_k} - \frac{\partial \langle u'_j \tau'_{ik} \rangle}{\partial x_k}}_{T^t} - \underbrace{2\nu \left\langle \frac{\partial u'_i}{\partial x_k} \frac{\partial u'_j}{\partial x_k} \right\rangle}_{\epsilon}, \tag{3.1}
 \end{aligned}$$

where A is the advection, D^v is the viscous diffusion, P^m is the production by the mean shear, P^w is the production by the wave-coherent motions, T^p is the pressure transport, R is the pressure–strain correlation, T^t is the spatial flux associated with turbulence and SGS stress, and ϵ is the dissipation. For the non-stationary turbulence field with the wind gust over the wave, each budget term is a function of two spatial coordinates (i.e. ξ and ζ) and the time.

To investigate the time evolution of a budget term, we perform the integration along both the ξ and ζ directions to evaluate its net contribution in the entire domain. For example, with the dissipation, we define

$$\check{\epsilon}_{ij}(t) = \frac{1}{L_x L_z} \int \epsilon_{ij}(\xi, \zeta) d\xi d\zeta, \tag{3.2}$$

where the integral, denoted by $\check{(\)}$, is performed in the whole computational domain (He & Seddighi 2013); alternatively, it can be computed separately in part of the domain (Lozano-Durán *et al.* 2020), e.g. in the buffer layer and the logarithmic layer. The net contributions of the other budget terms (\check{P}_{ij}^m , \check{R}_{ij} , etc.) are calculated following (3.2).

The time history of the net contributions for $\langle u'u' \rangle$ is shown in figure 6, where the dominant budget terms are plotted and the secondary terms are neglected for simplicity. The rapid change in the production by the mean shear \check{P}_{11}^m is a key contributor to the time variations of $\langle u'u' \rangle$. In both growing wind and decaying wind, there is a clear phase lag in the pressure–strain correlation \check{R}_{11} , compared with the production \check{P}_{11}^m and the dissipation $\check{\epsilon}_{11}$. The net contribution of the normal components of the pressure–strain correlation terms, \check{R}_{11} , \check{R}_{22} and \check{R}_{33} , to the TKE vanishes because their role is to redistribute the energy among the different normal Reynolds stress terms through the pressure. The direction of the energy transfer is predominantly from $\langle u'u' \rangle$ to $\langle v'v' \rangle$ and $\langle w'w' \rangle$, as indicated by the negative \check{R}_{11} in figure 6. Therefore, the delay of \check{R}_{11} compared with \check{P}_{11}^m explains the phase lag of $\langle w'w' \rangle$ with respect to $\langle u'u' \rangle$ (figure 5).

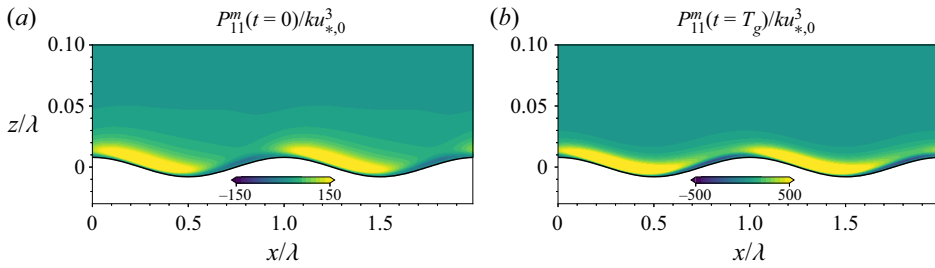


Figure 7. Turbulence production by the mean shear for the growing wind at (a) $t = 0$ and (b) $t = T_g$, in case CU8. Note that the contour magnitudes are different in (a) and (b).

To evaluate the wave-induced effect, we now examine the spatial distributions of the turbulence production associated with the mean shear, P_{11}^m , and the wave-coherent shear, P_{11}^w , defined in (3.1). As shown from comparison between figures 7(a) and 7(b), the magnitude of P_{11}^m increases drastically during the growing wind gust in case CU8, while the spatial distributions are unaffected. In particular, the positive peak values of P_{11}^m appear on the leeward side of the wave crest, which is similar to the steady wind turbulence in previous numerical studies (e.g. Yang & Shen 2010). A similar feature was observed for the total turbulence production in the tank experiment by Yousefi, Veron & Buckley (2021). Since the change in the turbulent stress is relatively small during the gust, the time variation of P_{11}^m is caused primarily by the mean shear evolution near the wave surface (figure 22). In the decaying wind case, the qualitative features of P_{11}^m are similar except that its magnitude decreases during the gust (results not plotted).

Figure 8 shows the spatial distribution of the turbulence production by the wave-coherent shear, P_{11}^w , in the growing wind. The wind gust induces a change in both the magnitude and spatial patterns of P_{11}^w , because of the variation in the wave-coherent shear $\partial \tilde{u}_i / \partial x_j$. The contours of P_{11}^w then show a strong dependency on the wave age. While the net contribution of P_{11}^w integrated over a wavelength at a constant ζ is small, it has a local magnitude of the same order as the mean-shear production P_{11}^m (see e.g. figures 7b and 8b), which imposes a strong modulation on the local turbulence field by the wave. For the decaying wind, the evolution of P_{11}^w is qualitatively a time reversal of figure 8 (not plotted). These transient features of P_{11}^w are associated closely with those of the wave-coherent velocity field, with more detailed analyses presented in § 3.3 below.

The locally axisymmetric turbulence hypothesis is an important aspect in the characterization of turbulent flows. According to the theory developed by George & Hussein (1991), one can validate the hypothesis by examining the relation between certain components of the mean square velocity gradient

$$\overline{\left(\frac{\partial u'_i}{\partial x_j}\right)^2} = \overline{\left(\frac{\partial u'_l}{\partial x_m}\right)^2}, \quad (3.3)$$

where $\overline{(\)}$ denotes the (combined) ensemble and plane averaging, and $(i, j, l, m) = (1, 2, 1, 3), (2, 1, 3, 1), (2, 3, 3, 2), (2, 2, 3, 3)$. Here, we assume that x_1 is the preferred local axis. To facilitate analysis, we first perform an interpolation in the vertical direction to transform the velocity field from the original boundary-fitted grid to a Cartesian grid where x_1, x_2 and x_3 correspond to the streamwise, spanwise and vertical directions. The velocity gradients are then calculated in regions above the wave crest. The ratios $\overline{(\partial u'_i / \partial x_j)^2} / \overline{(\partial u'_l / \partial x_m)^2}$ are qualitatively the same in all cases, and we present the results in

Gusty wind turbulence over a travelling wave

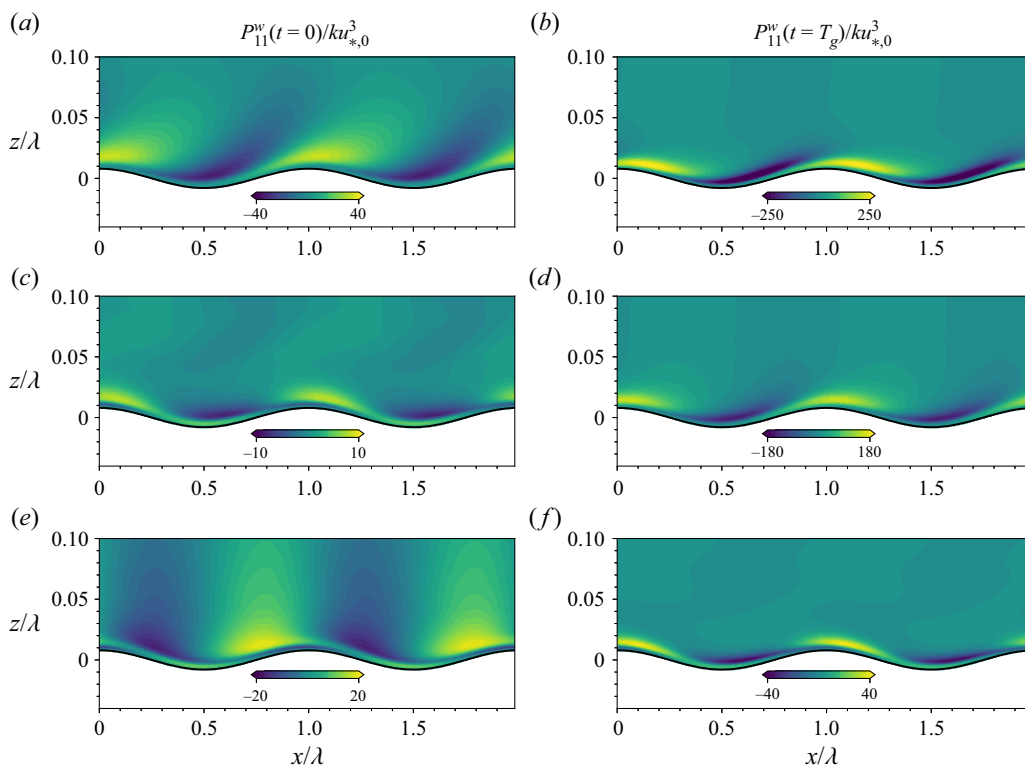


Figure 8. Turbulence production by the wave-coherent motions for the growing wind in (a,b) case CU8, (c,d) case CU19, and (e,f) case CU42. Plotted are the normalized values $P_{11}^w / k u_{*0}^3$ at $t = 0$ and $t = T_g$.

the growing wind for case CU8 as an example in figure 9. For an exact axisymmetric turbulent flow, all these ratios should be unity. In our simulation, their profiles show strong deviations from one below $z \sim O(0.1\lambda)$ (figure 9a). The time history of the ratios at $z \approx 0.1\lambda$ is shown in figure 9(b). Because of the memory effect in the turbulence response to the wind gust event, most $\overline{(\partial u'_i / \partial x_j)^2} / \overline{(\partial u'_l / \partial x_m)^2}$ are nearly unchanged at this height, except for the one with $(i, j, l, m) = (1, 2, 1, 3)$. We find that this phenomenon is caused mainly by a rapid change in $\overline{(\partial u'_1 / \partial x_3)^2}$ that is associated closely with the streamwise streak variation during the wind gust (see figure 2). The ratios corresponding to $(i, j, l, m) = (1, 2, 1, 3)$ and $(2, 3, 3, 2)$ satisfy the locally axisymmetric turbulence hypothesis with a 5% error, while for $(i, j, l, m) = (2, 1, 3, 1)$ and $(2, 2, 3, 3)$, the errors are larger (20%–40%). In general, the wind turbulence field shows a roughly local axisymmetry away from the wave surface. We remark that for wind turbulence over waves, the calculation of $\overline{(\partial u'_i / \partial x_j)^2}$ is non-trivial because of the wave-coherent motions (in the wind field) and the fluctuating surface, and therefore more systematic study is needed to examine whether (3.3) is a good indicator of a streaky turbulence structure.

We next consider the ratio between the turbulent stress components in the inner layer, which, according to Belcher & Hunt (1993), can be estimated from $T_D(z_i) = T_L(z_i)$. Here, z_i is the top of the inner layer, $T_D(z_i) = z_i / u_*$ is the eddy turnover time scale, and $T_L(z_i) = k / (U(z_i) - c)$ is the advection time scale for wind flow past a wavelength. During the wind gust, the inner layer thickness decreases from 0.076λ to 0.036λ for the growing wind, and increases from 0.043λ to 0.087λ for the decaying wind, in case CU8. To ensure that the

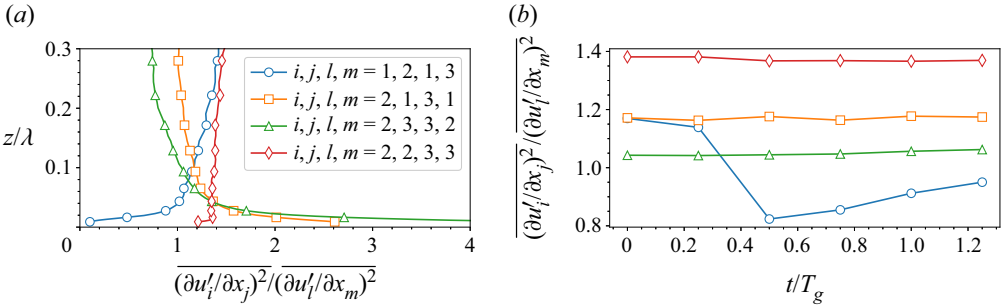


Figure 9. Ratios of the mean square velocity gradient in the growing wind for case CU8: (a) vertical profiles at $t = 0$; (b) time variations at height $z = 0.1\lambda$.

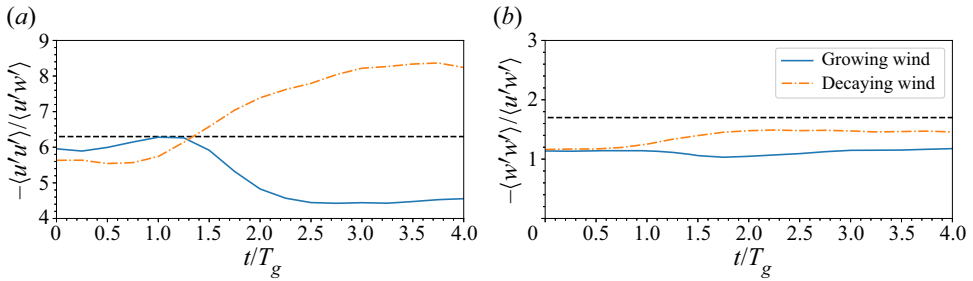


Figure 10. Time variations of the ratio of the turbulent normal stress to the turbulent shear stress at height $z = 0.036\lambda$ in case CU8. Also plotted are the values corresponding to an equilibrium boundary layer over a wave (Belcher & Hunt 1993): $-\langle u'^2 \rangle / \langle u'w' \rangle = 6.3$ and $-\langle w'^2 \rangle / \langle u'w' \rangle = 1.7$, denoted by the black dashed line.

analysis is performed in the inner layer, here we choose the fixed height at $z = 0.036\lambda$, which is close to the inner layer thickness found for wind turbulence at the wave age 6.5 in a tank experiment (Buckley & Veron 2016). Figure 10 shows the time variation of the ratio of the turbulent normal stress to the turbulent shear stress, which was assumed to be constant in the inner layer by Belcher & Hunt (1993) in their study of steady wind over waves. Our result, at the equilibrium state ($t = 0$), shows that the stress ratio is only slightly less than their recommended value. Similar to the turbulent stress, the stress ratio has a delayed response to the gust. While the time variation of $-\langle w'^2 \rangle / \langle u'w' \rangle$ is relatively small, the wind gust impact is significant for $-\langle u'^2 \rangle / \langle u'w' \rangle$ (note the different scalings of the vertical coordinates in figures 10a,b). In summary, we find that compared to statistically steady wind, the gust induces appreciable differences to the turbulence, and the delayed response to the gust event is a key feature of the transient behaviours of the turbulence field. The properties of the mean square velocity gradient indicate that the local axisymmetry may exist in the wind turbulence field away from the wave surface, while the (more restrictive) conditions for local isotropy are less likely to be satisfied.

3.3. Evolution of wave-coherent motions

This subsection focuses on the transient features of the wave-coherent streamwise velocity \tilde{u} , vertical velocity \tilde{w} and pressure \tilde{p} , which are useful for the quantitative analyses in the following subsections. We first illustrate \tilde{u} and \tilde{w} for the growing wind cases at the initial steady state $t = 0$ and the end of the gust $t = T_g$, as plotted in figure 11. For all three cases, the contour patterns of the wave-coherent motions under the unsteady wind condition are qualitatively similar to those under the steady wind condition, as long as their wave ages

Gusty wind turbulence over a travelling wave

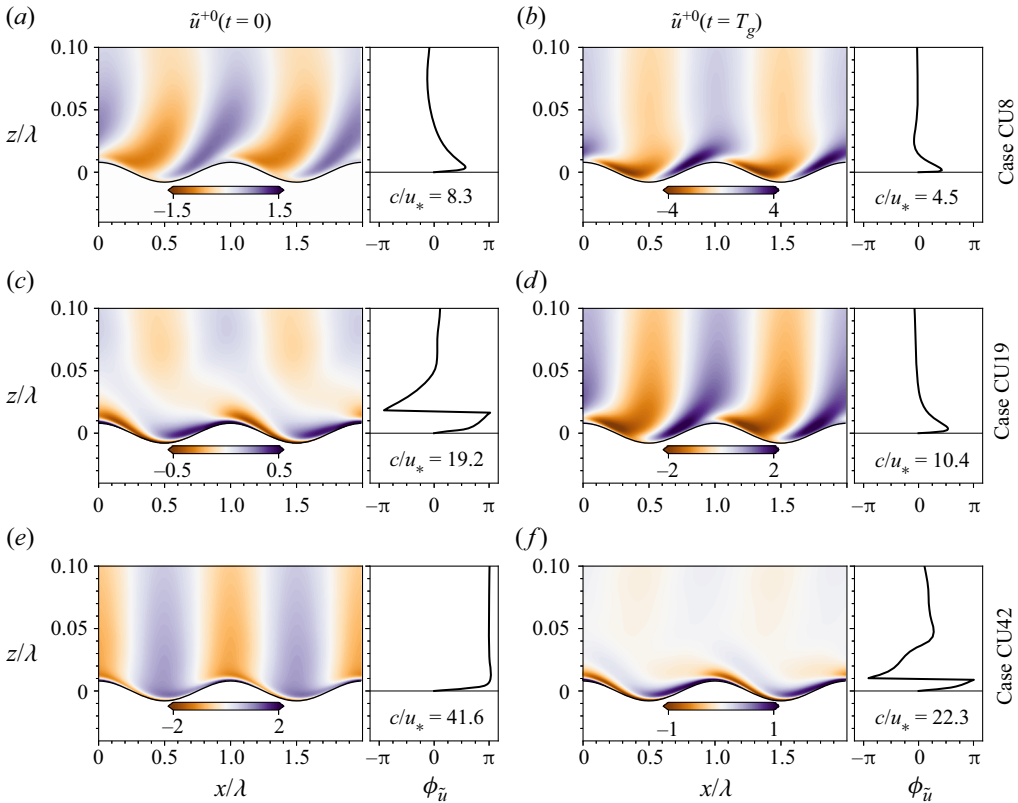


Figure 11. Wave-coherent streamwise velocity and its phase angle relative to the surface elevation for the growing wind in (a,b) case CU8, (c,d) case CU19, and (e,f) case CU42. The results are plotted at (a,c,e) $t = 0$ and (b,d,f) $t = T_g$. Also listed is the instantaneous wave age c/u_* . Here, \tilde{u} is normalized by $u_{*,0}$.

are in the same range. In the small wave age range ($c/u_* \sim 10$, see figures 11a,b,d), \tilde{u} shows the non-separated sheltering feature, which corresponds to a phase shift of $\pi/2$ near the wave surface. The distribution of \tilde{u} varies drastically with height near the wave surface. Because the wave ages throughout the gust event in case CU8 are in the same range, the contour shapes of \tilde{u} are qualitatively unchanged during the gust despite a significant increase in its magnitude (comparing figures 11a,b). In case CU19, the wave-coherent motions at $t = 0$ decrease rapidly with height, and overall their magnitudes are relatively small in most of the domain. For the wave age in this case, the gust event has a profound effect on both the magnitude and the contour pattern of the wave-coherent motions. Most notably, the contours of \tilde{u} near the wave surface are tilted towards the $-x$ direction at $t = 0$, and the $+x$ direction at $t = T_g$ (figures 11c,d). In the intermediate wave age, i.e. $c/u_* \sim O(20)$, the contour patterns correspond to a phase shift of 2π with the height from $z = 0$ to $z = 0.05\lambda$ (see figures 11c,f). Note that the discontinuity near $z = 0.01\lambda - 0.02\lambda$ is due to the definition of the phase angle, which limits $\phi_{\tilde{u}}$ between $-\pi$ and π . For the fast propagating wave at $t = 0$ in case CU42 (see figure 11e), \tilde{u} is nearly symmetric with respect to the wave surface except for a thin layer near the wave surface (for a similar pattern, see Cao & Shen 2021).

The distributions of \tilde{w} in the growing wind are plotted in figure 12. Compared with the streamwise velocity \tilde{u} with complex contour patterns, \tilde{w} exhibits relatively simple

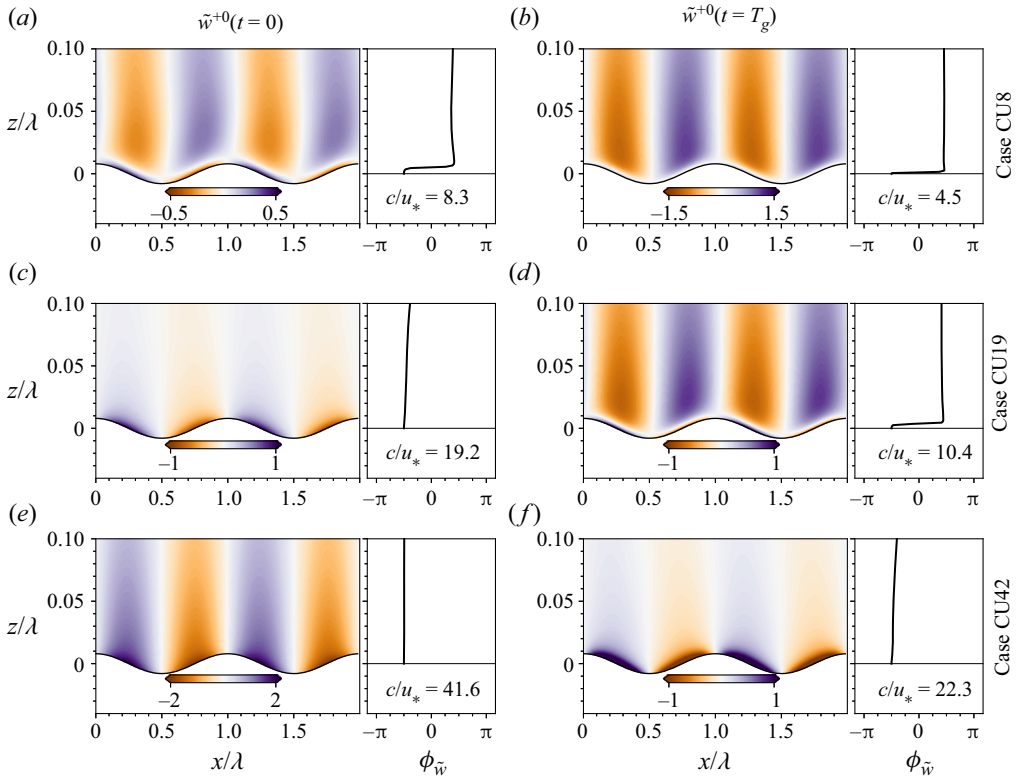


Figure 12. Same as figure 11, but for the vertical wave-coherent velocity \tilde{w} .

spatial distributions. Regardless of the wave age and the time instant, the imaginary part of \tilde{w} always dominates, i.e. $\phi_{\tilde{w}} \approx \pm\pi/2$ in the entire domain. When the wave age is not large (figures 12a,b,d), $\phi_{\tilde{w}}$ changes from $-\pi/2$ to $\pi/2$, while for the relatively large wave ages in figures 12(c,e,f), $\phi_{\tilde{w}}$ has a constant value close to $-\pi/2$ in the region $z < 0.1\lambda$. This feature of \tilde{w} agrees with the Miles (1957) theory based on the Rayleigh equation, which predicts the phase change across the critical layer. A brief review of the critical layer at the steady state can be found in Appendix C.

The evolution of the amplitudes of the wave-coherent motions in the growing wind is shown in figure 13. The vertical coordinates for $|\tilde{u}|$ and $|\tilde{w}|$ are plotted on a logarithmic scale to highlight the near-surface structures. In case CU8, $|\tilde{u}|$ and $|\tilde{w}|$ reach their peak values around $\zeta \sim O(10^{-2})\lambda$. In case CU42, $|\tilde{u}|$ and $|\tilde{w}|$ decrease nearly monotonically with the height except for $|\tilde{u}|$ at early times. In case CU19, the vertical distribution of the wave-coherent velocity amplitudes sees a transition from a monotonic function of height to a more complex pattern during the gust. The pressure amplitudes $|\tilde{p}|$ on the logarithmic scale are nearly straight lines with the same slope in most cases, following an $\exp(-k\zeta)$ decay with the height, especially when ζ is large. The only exceptions occur at $t = 0$ in case CU19 and $t = T_g$ in case CU42, where $|\tilde{p}|$ is prominent only at the wave surface. Away from the surface, the values of $|\tilde{p}|$ are too small and may be subject to fluctuations in the triple decomposition statistics. The velocity amplitudes show a similar exponential decay above $\zeta \sim O(10^{-2})\lambda$. The exponential decay of the wave-coherent motions is a well-known feature of the asymptotic inviscid solutions at large z (Belcher & Hunt 1993).

Gusty wind turbulence over a travelling wave

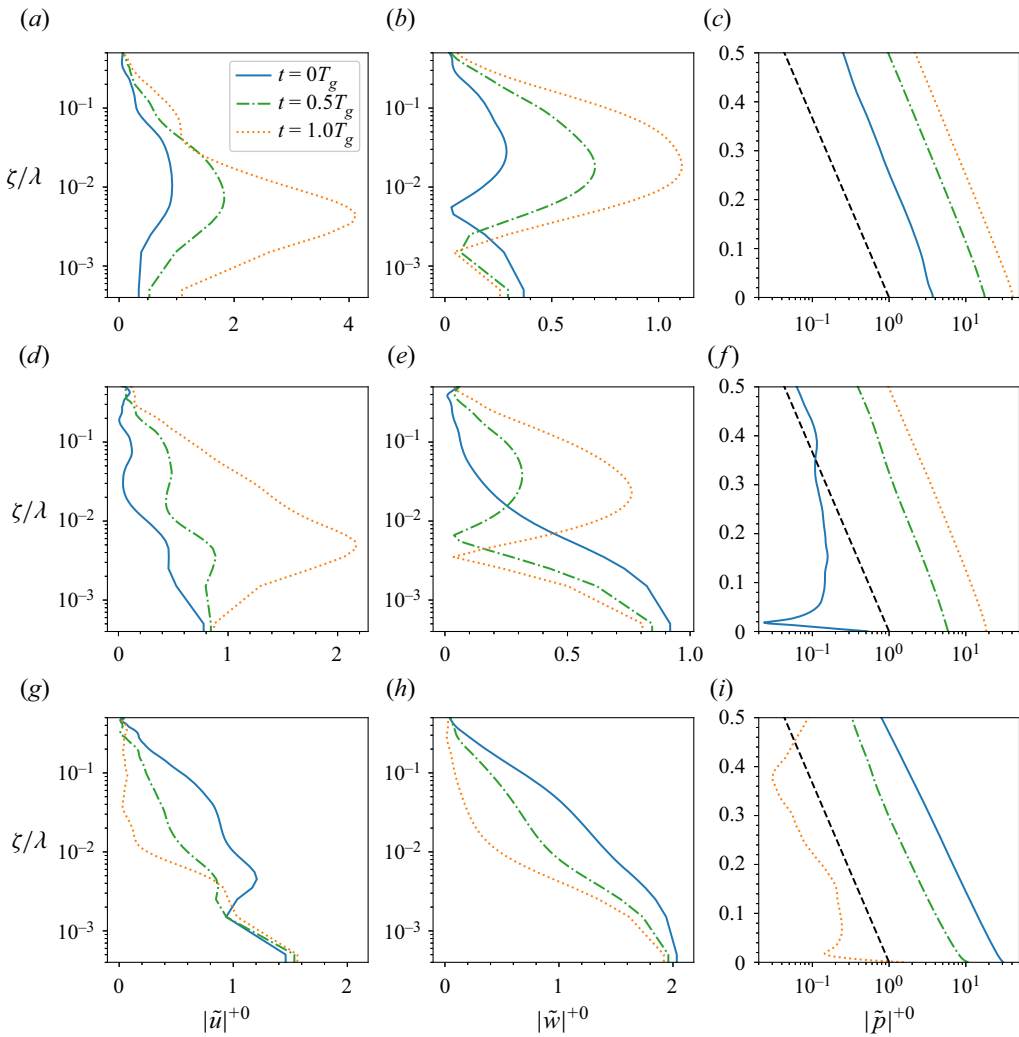


Figure 13. Vertical distributions of the amplitudes of the wave-coherent motions \tilde{u} , \tilde{w} and \tilde{p} for the growing wind in (a–c) case CU8, (d–f) case CU19, and (g–i) case CU42. The exponential decay $\exp(-k\zeta)$ is denoted by the black dashed lines. The results are plotted at $t/T_g = 0, 0.5, 1.0$. All terms are normalized using the wall unit at $t = 0$.

In contrast, a noticeable deviation from $\exp(-k\zeta)$ may be observed in the distribution of the pressure amplitude near the wave surface because of the wave geometry and the strong gradient in the vertical velocity, as suggested by previous studies (e.g. Yang & Shen 2010; Grare *et al.* 2013). As the mean velocity increases rapidly during the gust, the viscous effect is enhanced mostly in the thin region near the wave surface, as shown in figure 3. But the outer region remains approximately inviscid, and as a result, the exponential decay still holds there.

To identify the wave boundary layer, we plot separately the profiles of the turbulent and wave-coherent parts of the Reynolds shear stress (figure 14). The sign of $-\langle \tilde{u}\tilde{w} \rangle$ depends on the instantaneous wave age. For slow waves in case CU8 (figures 14a,d), the wave-coherent stress has an opposite sign to the turbulent part, which agrees with the findings of Hara & Sullivan (2015). For fast waves in case CU42 (figures 14c,f), their signs are the same.

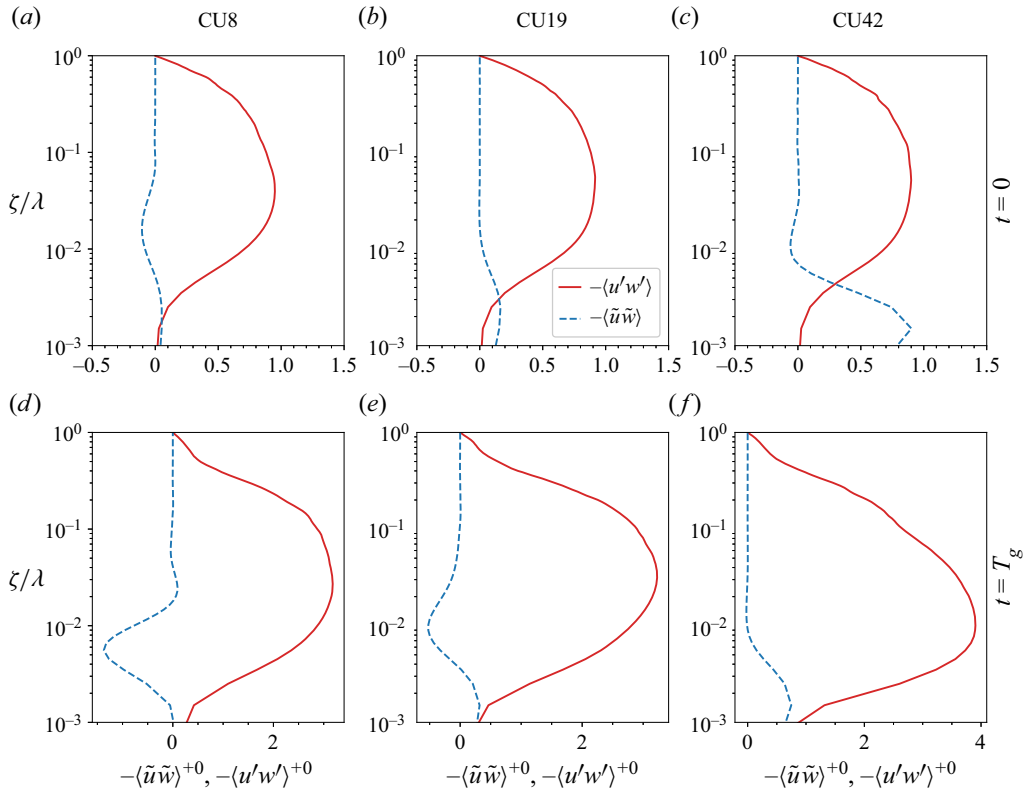


Figure 14. Turbulent and wave-coherent parts of the Reynolds shear stress for the growing wind at (a–c) $t = 0$ and (d–f) $t = T_g$. All terms are normalized using the wall unit at $t = 0$. The instantaneous wave ages for (a–f) are $c/u_* = 8.3, 19.2, 41.6, 4.5, 10.4, 22.3$, respectively.

The transition between these two patterns occurs at the wave age $c/u_* \sim 20$, as indicated by the results in case CU19 (figures 14b,e). When $-\langle \tilde{u}\tilde{w} \rangle$ is sufficiently large compared with $-\langle u'w' \rangle$ (figures 14c,d), the wave boundary layer is most distinguishable, with thickness $0.008\lambda - 0.02\lambda$ (see also the tank experiment by Buckley & Veron 2016).

To summarize, the wave-coherent motions can be identified clearly throughout our simulations, which justifies the use of the triple decomposition in the transient wind–wave process. Owing to page limits for the paper, the time series of the two-dimensional distributions of all wave-coherent components in both growing wind and decaying wind are depicted in the supplementary movies available at <https://doi.org/10.1017/jfm.2022.577>. A key feature that we see from figures 11–13 is that while the turbulent stresses exhibit the memory effect associated with the gust events (§ 3.2), the wave-coherent motions have a quasi-stationary response to the wind gust and they are strongly dependent on the instantaneous wave age. Furthermore, the growing wind gust has a counterintuitive phenomenon in case CU42: the wave-coherent motions are suppressed, i.e. their magnitudes at $t = T_g$ (figures 11f and 12f) are smaller than their values at $t = 0$ (figures 11e and 12e), while in a decaying wind their amplitudes increase. This phenomenon is explained in the following analysis based on the momentum equation.

3.4. Analysis of the wave-coherent momentum equation

To understand further the mechanisms that govern the evolution of the wave-coherent motions during wind gust, we perform more detailed analyses by resorting to the momentum equation. While an energy budget equation for the wave-coherent motions can also be derived in a way similar to the TKE equation (3.1), the phases of the source terms would be complicated because of the product of trigonometric functions. The momentum equation, on the other hand, has a simpler form and preserves directly the phases of the wave-coherent motions. By performing the triple decomposition, the vertical wave-coherent momentum equation can be written as

$$\frac{\partial \tilde{w}}{\partial t} = \underbrace{-(U - c) \frac{\partial \tilde{w}}{\partial \xi}}_{\mathcal{A}} - \underbrace{\frac{\partial \tilde{u}'w'}{\partial \xi}}_{\mathcal{T}} - \underbrace{\frac{1}{\rho} \frac{\partial \tilde{p}}{\partial \xi}}_{\mathcal{P}} + \underbrace{\nu \nabla^2 \tilde{w}}_{\mathcal{V}}, \tag{3.4}$$

where \mathcal{A} , \mathcal{T} , \mathcal{P} and \mathcal{V} denote the effects of advection, turbulence, pressure gradient and viscosity, respectively. The effect of the wave-coherent stresses $\tilde{u}_i \tilde{u}_j$ ($i, j = 1, 3$) is omitted because they have a direct impact on the second harmonic wavenumber $4\pi/\lambda$ instead of the primary wavenumber $2\pi/\lambda$, and thus have little effect on the evolution of \tilde{w} . Apparently, the advection term \mathcal{A} and the pressure gradient term \mathcal{P} have rapid responses to the wind gust because they are determined by the mean velocity and the wave-coherent motions. The turbulence term \mathcal{T} , on the other hand, shares a similar memory effect with $\tilde{u}'w'$.

Similar to the decomposition of the wave-coherent motions shown in (2.6), the real part and the imaginary part of each term in the vertical momentum equation (3.4) can be calculated. Figure 15 shows the results for the real parts at $t = 0.5T_g$. Note that the viscous term is found to be negligibly small and has been omitted. In all three cases, the pressure gradient and the advection terms are significant in balancing the real part of (3.4). The turbulence effect nearly vanishes in case CU42. For cases CU8 and CU19, the effect of the turbulence term $\text{Re}[\mathcal{T}]$ is relatively strong in the decaying wind, while in the growing wind it is relatively weak. This phenomenon is similar to the time variation of the turbulence intensity discussed in § 3.1, and is also associated with the memory effect of the turbulent stress, which leads to a phase lag in $\text{Re}[\mathcal{T}]$ with respect to the rapidly varying $\text{Re}[\mathcal{A}]$ and $\text{Re}[\mathcal{P}]$. The temporal growth rate $\text{Re}[\partial \tilde{w}/\partial t]$ is negligibly small in all cases, suggesting that the real parts are largely balanced regardless of the gust event.

In contrast to the relatively simple distributions of the real parts of the terms in (3.4), the distributions of the imaginary parts are more complex, as shown in figure 16. The imaginary part of the viscous term, compared with its real part, is important in the vertical momentum equation near the wave surface, because $\text{Im}[\mathcal{V}] = \nu \nabla^2 \text{Im}[\tilde{w}]$, and $\text{Im}[\tilde{w}]$ dominates over $\text{Re}[\tilde{w}]$ (figure 12). In general, for the imaginary part, the values of different terms in (3.4) are of the same order, especially in case CU8. Unlike $\text{Re}[\partial \tilde{w}/\partial t]$, which is close to zero, $\text{Im}[\partial \tilde{w}/\partial t]$ becomes positive in the growing wind and negative in the decaying wind. Hence $\text{Im}[\partial \tilde{w}/\partial t]$ is the main contributor to the contour pattern changes presented in figure 12. In particular, for the growing wind in case CU42, $\text{Im}[\tilde{w}]$ at $t = 0$ is negative, noticing that $\text{Im}[\tilde{w}] = |\tilde{w}| \sin \phi_{\tilde{w}} < 0$ when $\phi_{\tilde{w}} \approx -\pi/2$ (see figure 12e). The positive $\partial \text{Im}[\tilde{w}]/\partial t$ then causes a magnitude reduction in $\text{Im}[\tilde{w}]$ during the growing wind event, which is confirmed in figures 12(e,f).

While the time variation in \tilde{w} is dominated by $\text{Im}[\partial \tilde{w}/\partial t]$, the real and imaginary parts of the momentum equation (3.4) are not independent of each other but dynamically coupled through the differential operator $\partial/\partial \xi$. For the advection term and the turbulence term, we

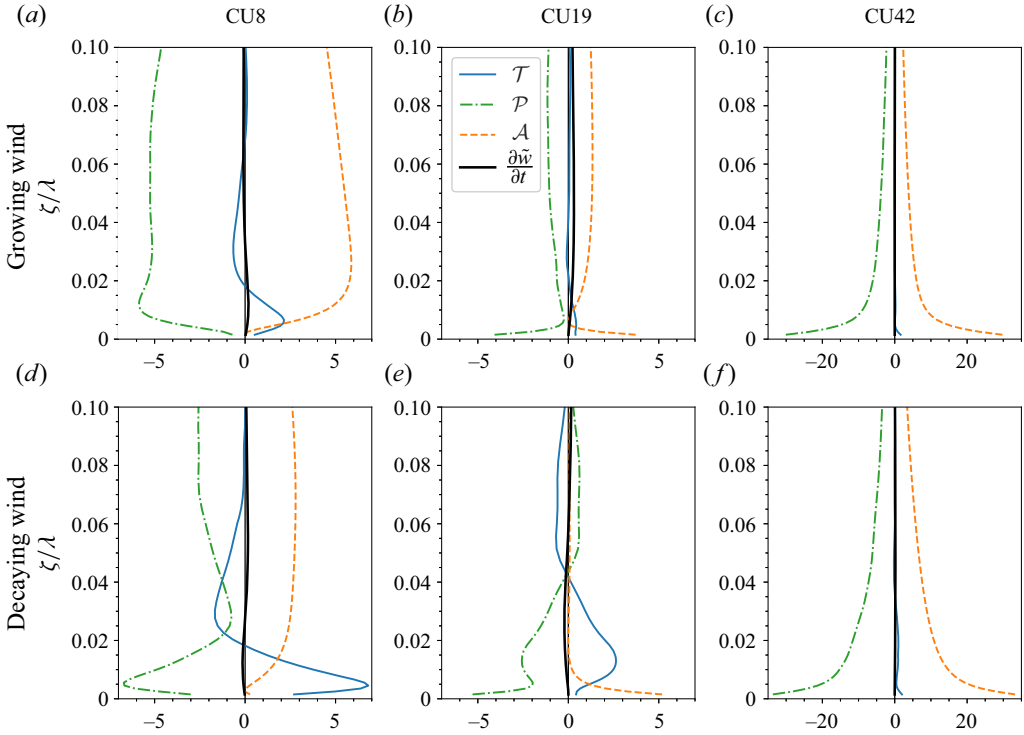


Figure 15. Real part of the terms in the vertical wave-coherent momentum equation for (a–c) the growing wind and (d–f) the decaying wind, at $t = 0.5T_g$. The instantaneous wave ages are $c/u_* = 5.1, 11.7, 25.2, 7.1, 16.6, 35.2$ in (a–f), respectively. All terms are normalized by $ku_{*,0}^2$.

have

$$\text{Re}[\mathcal{A}] = k(U - c) \text{Im}[\tilde{w}], \tag{3.5}$$

$$\text{Im}[\mathcal{A}] = -k(U - c) \text{Re}[\tilde{w}], \tag{3.6}$$

$$\text{Re}[\mathcal{T}] = k \text{Im}[\widetilde{u'w'}], \tag{3.7}$$

$$\text{Im}[\mathcal{T}] = -k \text{Re}[\widetilde{u'w'}]. \tag{3.8}$$

In case CU42, for instance, $\text{Re}[\mathcal{A}]$ (figures 15c,f) is much larger than $\text{Im}[\mathcal{A}]$ (figures 16c,f) because the wave-coherent vertical velocity is dominated by the out-of-phase imaginary part $\text{Im}[\tilde{w}]$ (see figure 12).

Next, we perform a quantitative analysis of the wave-coherent motions by utilizing and comparing with the viscous curvilinear model proposed by Cao *et al.* (2020). The model originates from the triple decomposition of the Navier–Stokes equations for wind turbulence over a monochromatic wave under the steady wind–wave condition. In their derivation, the nonlinear terms associated with the turbulent stress and the second-order terms of $O((ka)^2)$ related to the grid transformation are neglected. The governing equation for the vertical wave-coherent velocity \tilde{w} reads

$$\begin{aligned} & -\frac{\nu}{ik} \left(\frac{d^4}{d\xi^4} - 2k^2 \frac{d^2}{d\xi^2} + k^4 \right) \mathcal{F}[\tilde{w}] + \left[(U - c) \left(\frac{d^2}{d\xi^2} - k^2 \right) - \frac{d^2 U}{d\xi^2} \right] \mathcal{F}[\tilde{w}] \\ & = \mathcal{F} \left[\frac{\partial}{\partial t} \left(\frac{\partial \tilde{u}}{\partial \xi} - \frac{\partial \tilde{w}}{\partial \xi} \right) \right] + \nu \mathcal{F}[\eta] \frac{d^2}{d\xi^2} \left[\left(\frac{\xi}{h} - 1 \right) \frac{d^2 U}{d\xi^2} \right], \end{aligned} \tag{3.9}$$

Gusty wind turbulence over a travelling wave

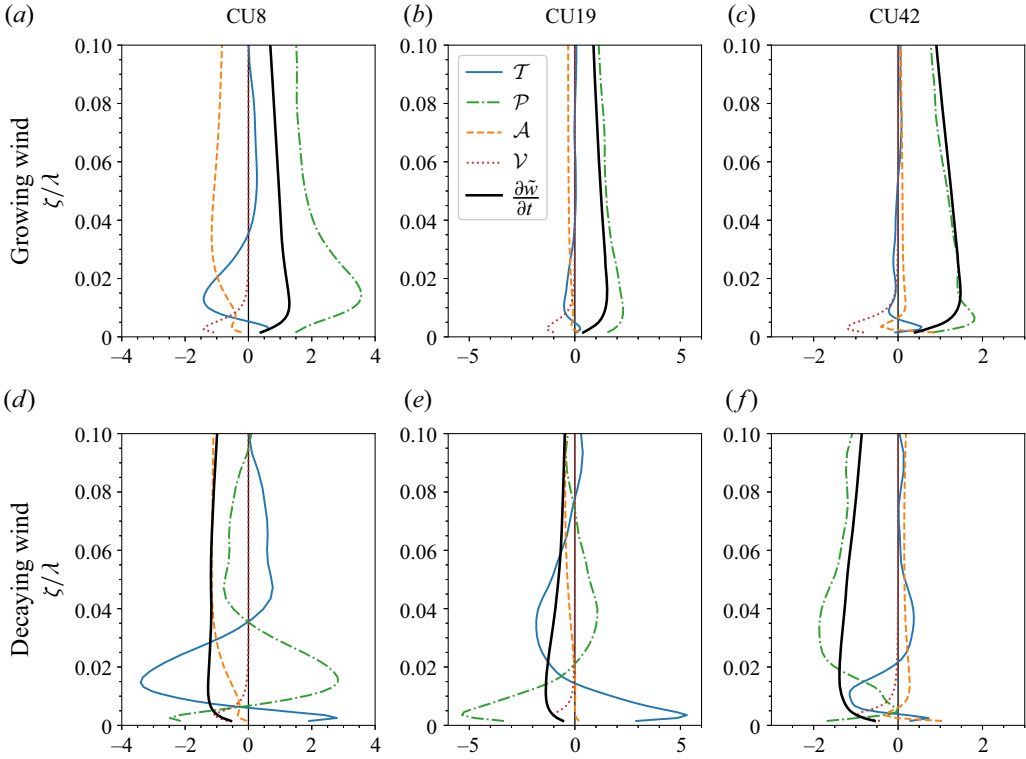


Figure 16. Same as figure 15, but for the imaginary parts.

where \mathcal{F} denotes the Fourier transform operator. For completeness, we keep the time derivative term that was neglected by Cao *et al.* (2020). But its actual value is also found to be insignificant compared with the other terms in the present wind gust cases. The mean profile $U(\zeta)$ is provided by the simulation, and the boundary conditions are

$$\tilde{w}(\zeta = 0) = w_s, \quad \tilde{w}(\zeta \rightarrow \infty) = 0, \tag{3.10a,b}$$

$$\left. \frac{d\tilde{w}}{d\zeta} \right|_{\zeta=0} = -\frac{du_s}{d\xi} + \frac{dU}{d\zeta} \frac{d\eta}{d\xi}, \quad \left. \frac{d\tilde{w}}{d\zeta} \right|_{\zeta \rightarrow \infty} = 0, \tag{3.11a,b}$$

where u_s and w_s are the streamwise and vertical wave orbital velocities, respectively (see Appendix A).

Here, the Dirichlet boundary condition for \tilde{w} at $\zeta = 0$ is prescribed by the wave orbital velocity, and its derivative $d\tilde{w}/d\zeta$ is obtained from the continuity equation. In practice, the top boundary condition ($\zeta \rightarrow \infty$) can be evaluated at a height where the magnitude of \tilde{w} is sufficiently small, say $\zeta = 0.5\lambda$ (Cao *et al.* 2020). Near the wave surface, the imaginary part of the vertical wave-coherent velocity dominates over the real part because of the $\pi/2$ phase difference between the vertical wave orbital velocity and the surface elevation (see (A6)).

In figure 17, we present $\text{Im}[\tilde{w}]$ at three instants in the growing wind gust. The evolution of $\text{Im}[\tilde{w}]$ dominates the qualitative features shown in figure 12. For example, the phase change of π in the vicinity of the wave surface in case CU8 (figure 12a) corresponds to the

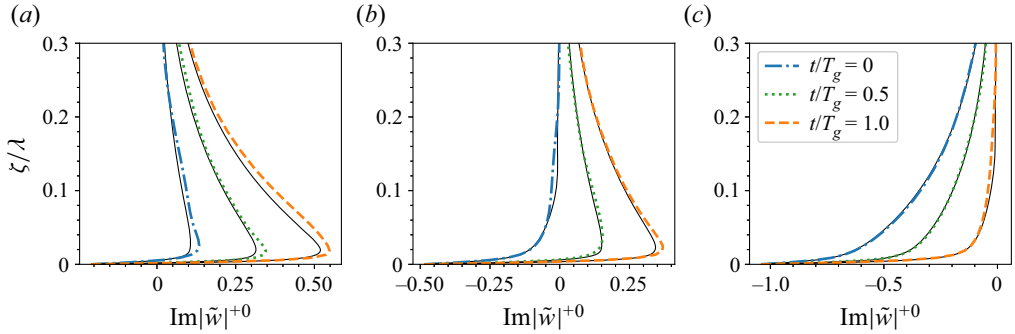


Figure 17. Imaginary part of the vertical wave-coherent velocity for the growing wind in (a) case CU8, (b) case CU19, and (c) case CU42. Also plotted are the corresponding results computed from the viscous curvilinear model, denoted by the black solid lines.

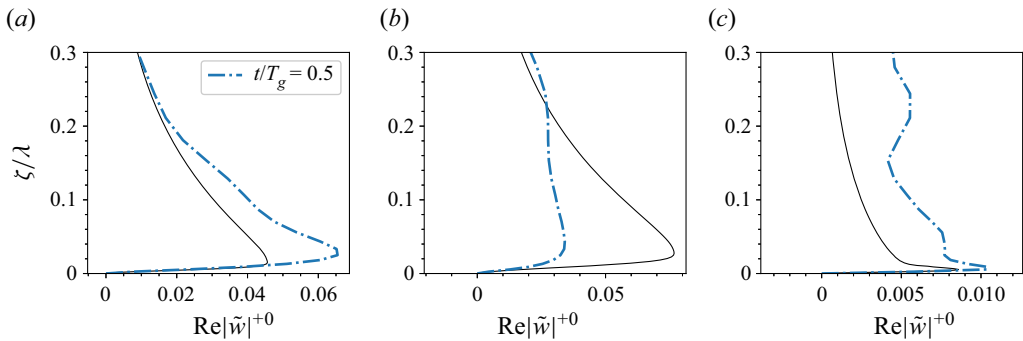


Figure 18. Real part of the vertical wave-coherent velocity for the growing wind in (a) case CU8, (b) case CU19, and (c) case CU42. The results computed from the viscous curvilinear model are denoted by the black solid lines.

sign reversal at small ζ/λ in figure 17(a). Consistent with the positive $\partial \text{Im}[\tilde{w}]/\partial t$ shown in figure 17, $\text{Im}[\tilde{w}]$ increases with the growing wind in all cases (figure 12). In general, the LES result agrees well quantitatively with the model prediction at both the steady state ($t = 0$) and the non-equilibrium state ($t = 0.5T_g$ and $t = T_g$). Hence the quasi-linear mechanism (Cao *et al.* 2020) that governs the response of $\text{Im}[\tilde{w}]$ to the mean velocity profile U is effective even under the gusty condition.

For $\text{Re}[\tilde{w}]$, on the other hand, the difference between the model prediction and the LES result is noticeable. In figure 18, we plot the instantaneous result at $t = 0.5T_g$ as an example. Qualitatively, the result predicted by the model has a shape similar to the LES result, in which $\text{Re}[\tilde{w}]$ first increases with the height and then decreases after reaching a positive peak value. The modelling of $\text{Re}[\tilde{w}]$ is challenging because it has a small magnitude compared with $\text{Im}[\tilde{w}]$. At $t = 0.5T_g$, the peak value of $\text{Re}[\tilde{w}]$ is approximately one-fifth of the corresponding value of $\text{Im}[\tilde{w}]$ in case CU8 (comparing figures 17a and 18a). At larger wave ages in case CU42, the difference between the magnitudes of $\text{Im}[\tilde{w}]$ and $\text{Re}[\tilde{w}]$ can be as large as two orders of magnitude (figures 17c and 18c). The viscous curvilinear model fails to predict the weak $\text{Re}[\tilde{w}]$ because the impacts of the turbulence and second-order terms omitted in the derivation of the model are no longer negligible.

Gusty wind turbulence over a travelling wave

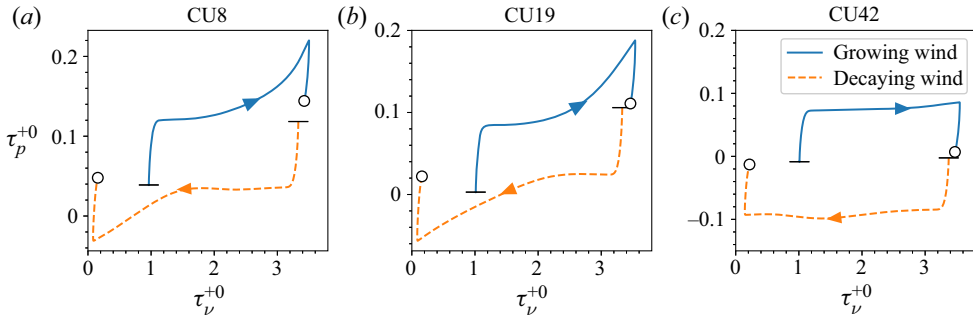


Figure 19. Evolution of form drag and viscous drag during the wind gust ($0 < t < T_g$). The start ($t = 0$) and end ($t = T_g$) of the gust are denoted by dash marks (–) and circles, respectively, and the arrows denote the direction of time increase.

From the analyses in this subsection, we obtain a clear picture of the wave-coherent motions. First, compared with the turbulent stress, the wave-coherent motions respond instantly to the gust event and show strong dependency on the wave age. Besides, the gust event leads to a drastic change in the out-of-phase component $\text{Im}[\tilde{w}]$, and has little impact on the in-phase component $\text{Re}[\tilde{w}]$. In the next subsection, we investigate whether these phenomena are responsible for producing the drag hysteresis that has been observed in laboratory and field experiments (Waseda *et al.* 2001; Hwang *et al.* 2011) and how the change in $\text{Im}[\tilde{w}]$ contributes to the variation in wind–wave energy transfer.

3.5. Wind gust impact on wave growth

It is well recognized that the wave-coherent motions play a critical role in the wind–wave momentum and energy transfer. In this subsection, we investigate how their time variations affect these processes. We first examine the evolution of the form drag τ_p and viscous drag τ_ν . In the present study, we use the sign convention such that the drags are positive when the direction of the momentum flux is from the wind to the wave, such as at small wave ages. As shown in figure 19, the viscous drag τ_ν changes continuously during the gust and remains positive. In all cases, τ_ν at the end of the growing wind gust is slightly larger than that at the start of the decaying wind gust, while at the end of the decaying gust, τ_ν nearly vanishes and is significantly smaller than its initial value in a growing wind. This hysteresis effect exhibited by τ_ν is associated primarily with the evolution of the mean velocity profile and the mean shear. As discussed in § 3.1, the uniform change in the mean velocity caused by the external force occurs mainly in the outer region where the mean shear is expected to be roughly unchanged during the gust. The near-wall region is dominated by viscosity such that the mean velocity and its gradient are affected by their past states.

The form drag τ_p sees an abrupt change at the start and end of the gust. During the wind gust, the variations in τ_p are relatively small at first, and this feature is shared in all cases. Near the end of the gust, there is a substantial change in τ_p for cases CU8 and CU19, while in case CU42 the change in τ_p is trivial. To understand the behaviours of τ_p , we consider its definition:

$$\tau_p = \frac{1}{L_x} \int_0^{L_x} \frac{p\eta_x}{\rho} dx = \frac{ka \text{Im}[\tilde{p}]|_{\zeta=0}}{\rho}. \quad (3.12)$$

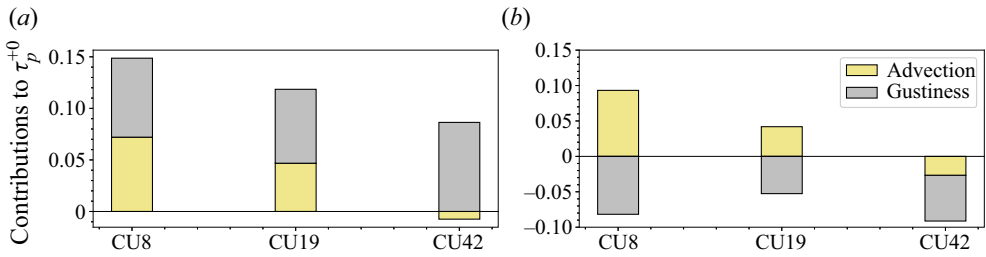


Figure 20. Contributions of the advection and gustiness terms to the form drag in (a) the growing wind and (b) the decaying wind. All terms are calculated by taking the time average during $0 < t < T_g$.

The pressure at the wave surface can be obtained by integrating the imaginary part of the vertical momentum equation (3.4). Keeping only the dominant terms, we can rewrite (3.12) as

$$\tau_p = ka \int_0^\lambda k(U - c) \operatorname{Re}[\tilde{w}] d\zeta + ka \int_0^\lambda \frac{\partial}{\partial t} \operatorname{Im}[\tilde{w}] d\zeta. \quad (3.13)$$

The contribution to the form drag is then decomposed into two parts, the advection of $\operatorname{Re}[\tilde{w}]$ and the time variation of $\operatorname{Im}[\tilde{w}]$ caused by the wind gust. For a wind turbulence field at the steady state, only the advection term needs to be included in the calculation, while the gustiness term reduces to zero (see e.g. Cao *et al.* 2020).

When the wind is unsteady, the gustiness term becomes important. In figure 20, we plot the time-averaged contributions from the advection and gustiness terms to the form drag during $0 < t < T_g$. For the advection term, the contribution varies with the wave age, which determines the advection velocity $U - c$. For the contribution by the gustiness, however, the wave age has less influence because the magnitudes of $\partial \operatorname{Im}[\tilde{w}] / \partial t$ are comparable in different cases (see figure 16). Figure 20 shows that in all cases, the gustiness term is comparable to (cases CU8 and CU19) or stronger than (case CU42) the advection term. Therefore, the out-of-phase component $\operatorname{Im}[\tilde{w}]$ that changes rapidly during the gust plays an at least equally important role as the in-phase component $\operatorname{Re}[\tilde{w}]$ in the wind–wave momentum transfer.

We now revisit figure 19 to explain the behaviour of τ_p based on the decomposition (3.13). The abrupt change immediately after $t = 0$ and before $t = T_g$ is caused by the contribution of the gustiness term. During $0 < t < T_g$, cases CU8 and CU19 have a noticeable change in τ_p because the advection term itself is changing with the mean velocity, and its contribution is comparable to that of the gustiness term (figure 20). For case CU42, although the mean velocity and the advection term change substantially during the wind gust, the magnitude of the advection term is much smaller than that of the gustiness term, as shown in figure 20. Therefore, the value of τ_p is relatively invariant during this process.

To quantify the amount of wind energy transferred to wave, we calculate the wave growth rate β (Miles 1957) and the temporal energy growth rate γ (Donelan & Pierson 1987):

$$\beta = \frac{2\tau_p}{(aku_*)^2}, \quad (3.14)$$

$$\gamma = \left(\frac{u_*}{c}\right)^2 \beta = \frac{2\tau_p}{(akc)^2}. \quad (3.15)$$

Case	Gust event	$\bar{\beta} = (2/a^2k^2)(\overline{\tau_p/u_*^2})$	$\bar{\gamma} = 2\overline{\tau_p}/(akc)^2$	$ \Delta U/U /\omega T_g$
CU8	Growing	46.9	1.7	0.31
	Decaying	9.6	0.27	0.38
CU19	Growing	36.6	0.25	0.13
	Decaying	-3.0	-0.0089	0.16
CU42	Growing	23.5	0.034	0.06
	Decaying	-51.0	-0.040	0.07

Table 3. Time-averaged β and γ during $0 < t < T_g$. Here, $\overline{(\)}$ is the time-averaging operator. Also listed is the strength of the gust event $|\Delta U/U|/\omega T_g$, where $\Delta U/U = [U(0.02\lambda, T_g) - U(0.02\lambda, 0)]/U(0.02\lambda, 0.5T_g)$ is the relative change in the mean profile, and ω is the wave frequency.

In table 3, we list the time-averaged results of β and γ during the wind gust ($0 < t < T_g$). We follow Miles & Ierley (1998) to obtain $\bar{\beta}$ by calculating separately the mean form drag and the average of the square of the friction velocity, and then using them to calculate $\bar{\beta}$. For both $\bar{\beta}$ and $\bar{\gamma}$, there is a distinct difference between the growing wind result and the decaying wind result. The primary reason for this difference is due to the hysteresis phenomenon in the variation of the form drag and the viscous drag (figure 19).

We plot β as a function of the wave age c/u_* in figure 21(a). The results denoted by the light grey and dark grey symbols are instantaneous values at $t = 0$, while those during the gust, denoted by coloured symbols, are calculated as the time-averaged values (see table 3). At the steady state before the gust event occurs, β varies with the wave age and is in general consistent with the results in the literature (Sullivan *et al.* 2000; Kihara *et al.* 2007; Yang & Shen 2010; Druzhinin *et al.* 2012; Åkervik & Vartdal 2019). When the wind gust starts, there is an immediate change in the wave age associated with the time-varying friction velocity u_* (see the evolution of the friction drag in figure 19). The shift in the wave age has been incorporated into the wind input source terms in phase-averaged wave models to account for the gustiness effect on the wave energy growth (Janssen 2004). For atmospheric variability with a time scale much larger than the wave period and the wind turbulence in a quasi-equilibrium state, this simple approximation is likely appropriate. But more generally, especially for a rapidly changing wind field, this is not the case. Our result in figure 21(a) shows a noticeable deviation of $\bar{\beta}$ from the steady state value. The strength of the wind gust can be measured roughly by $|\Delta U/U|/\omega T_g$ (table 3), or, more generally, $(\partial U/\partial t)/\omega|U|$ (see Miles & Ierley 1998). Note that while by this definition the wind gust event is the weakest in the high wave age case CU42, the deviation of β from the steady-state values is most significant in this case because the gustiness effect has the largest relative contribution to the form drag (see figure 20).

In figure 21(b), we plot γ using an alternative scaling based on $U_{\lambda/2}$, the characteristic mean velocity at $\zeta = \lambda/2$ (Donelan *et al.* 2006). The steady-state values are consistent with the parametrization proposed by Donelan *et al.* (2006), $\gamma = 0.17$. While this parametrization is effective in reducing the scattering compared with the scaling based on u_* shown in figure 21(a), it underestimates γ in the growing wind and overestimates γ in the decaying wind. The deviation, which can be up to several orders of magnitude, is a consequence of the change in the mean velocity $U_{\lambda/2}$ and γ itself. Therefore, the non-stationary effect associated with the wind gust cannot be incorporated into such parametrized wind input models by simply using a shift in the wave age $c/U_{\lambda/2}$. More research on the model development, which is beyond the scope of this work, is called for in future studies.

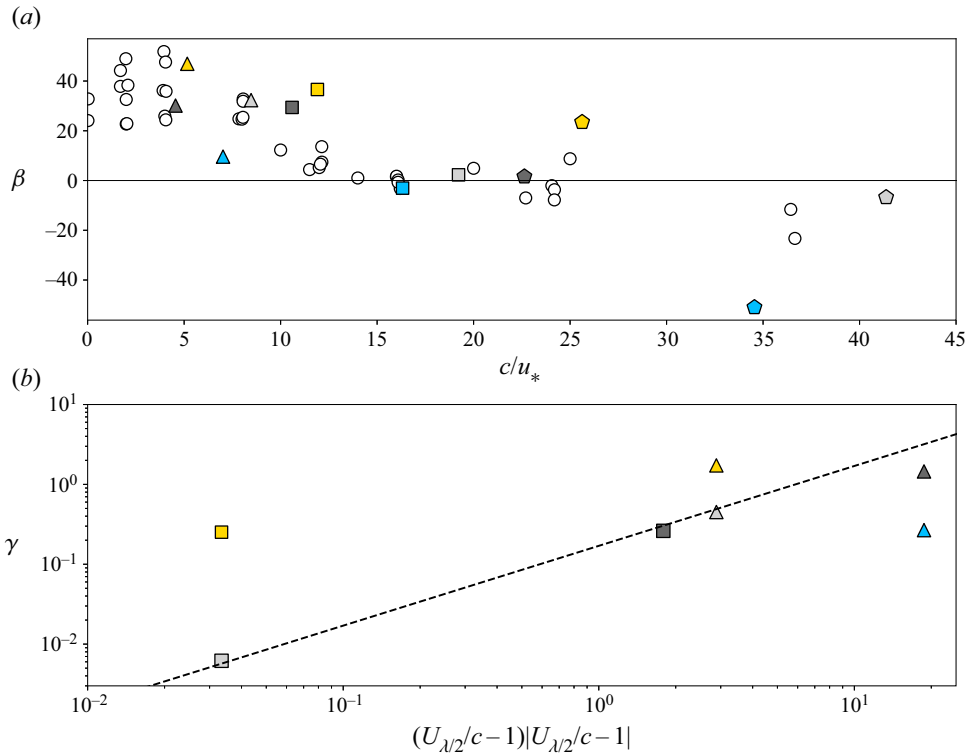


Figure 21. (a) Wave growth rate β scaled with the friction velocity u_* . (b) Temporal growth rate γ scaled with the mean wind velocity at the height of half-wavelength $U_{\lambda/2}$. In (a), the results in cases CU8, CU19 and CU42 are denoted by triangles, squares and pentagons, respectively. The symbols with the filled colours light grey and dark grey denote the initial steady-state results, and those with the colours gold and blue are the time-averaged values $\bar{\beta}$ during the growing wind and the decaying gust, respectively. Also plotted are the steady-state results with similar wave steepness ($ak < 0.1$) obtained using direct numerical simulation (Sullivan *et al.* 2000; Kihara *et al.* 2007; Yang & Shen 2010; Druzhinin *et al.* 2012) and LES (Åkervik & Vartdal 2019), denoted by circles. In (b), only those results with positive values of γ and $U_{\lambda/2}/c - 1$ are plotted. The black dashed line denotes the parametrization proposed by Donelan *et al.* (2006): $\gamma = 0.17(U_{\lambda/2}/c - 1)|U_{\lambda/2}/c - 1|$.

4. Concluding remarks

In this study, we have performed high-resolution wall-resolved LES of wind turbulence over a travelling wave, where the wind field is subject to an impulsive growing and decaying gust event. Multiple wave speeds are designed to cover representative wave ages. Compared with the vast majority of current research that assumes a stationary or quasi-stationary state for the wind–wave interaction, we investigate the non-stationary state of wind turbulence, which exists widely in the atmospheric boundary layer above ocean waves. This study focuses on the transient features of the turbulent and wave-coherent motions as well as their impact on the momentum and energy transfer.

We show that the turbulence fluctuations have a delayed response to the mean shear, similar to classical channel flow results. We find that this memory effect is caused mainly by the phase delay in the production induced by the mean shear, the pressure–strain correlation and the dissipation. On the other hand, the wave-coherent motions and the associated production are found to have a quasi-stationary response to the gust: the qualitative features of the wave-coherent motions during the wind gust are similar to

those in a steady wind turbulence with the same instantaneous wave age. By evaluating the terms in the wave-coherent vertical momentum equation, we find that the component of the vertical wave-coherent velocity \tilde{w} out of phase with the surface elevation, $\text{Im}[\tilde{w}]$, dominates the change in \tilde{w} , while the in-phase component, $\text{Re}[\tilde{w}]$, has a much smaller temporal growth rate. We show that as a result of the quasi-stationary response, $\text{Im}[\tilde{w}]$ can be predicted by the viscous curvilinear model developed originally for steady state, even during the wind gust event, while $\text{Re}[\tilde{w}]$ cannot be predicted, owing to the relatively small amplitude.

We have also investigated the effect of wind gust on wind–wave momentum and energy transfer. The evolution of the form drag and the viscous drag demonstrates a hysteresis phenomenon and presents a distinct difference between the growing and decaying wind. We have identified $\partial\text{Im}[\tilde{w}]/\partial t$ as a key contributor to the form drag (and thus the wave growth) during wind gust. Our result also shows that this contribution from the out-of-phase component $\text{Im}[\tilde{w}]$ is comparable to that caused by the advection of the in-phase component $\text{Re}[\tilde{w}]$ at low and intermediate wave ages, and much stronger at a high wave age.

A major implication of the discovery of the transient behaviours of turbulence in wind gust is associated with the closure model of the Reynolds stress. The local turbulence equilibrium assumption used in the classical wind–wave growth theories is no longer valid. Therefore, the wind gustiness effect poses significant challenges to the modelling of the non-equilibrium turbulent stresses, for which more research is needed. From a more practical perspective, our discovery shows the necessity to incorporate the transient features of the wind field into the wind input models in operational wave models. Such improvement may also be helpful in reducing the large scattering found in the wave growth rate from field observations, which is plotted against the wave age alone, typically, but without considering the transient effect. Finally, we remark that the simulation set-up in the present study is relatively simple, limited by the computational cost needed for resolving the viscous sublayer and performing the ensemble runs. More realistic marine conditions, such as irregular waves and dynamical coupling between wind and waves, should be taken into consideration in future studies.

Supplementary movies. Supplementary movies are available at <https://doi.org/10.1017/jfm.2022.577>.

Acknowledgements. The authors gratefully acknowledge the referees for their constructive and valuable comments.

Funding. This work is supported by the Office of Naval Research.

Declaration of interests. The authors report no conflict of interest.

Author ORCIDs.

 Xuanting Hao <https://orcid.org/0000-0003-4898-1074>;

 Lian Shen <https://orcid.org/0000-0003-3762-3829>.

Appendix A. Wind turbulence solver

The numerical solver developed originally by Yang & Shen (2011*a,b*) has been used extensively and validated in studies on wind–wave interaction (e.g. Yang *et al.* 2013; Hao & Shen 2019; Cao *et al.* 2020; Cao & Shen 2021). The filtered Navier–Stokes equations (2.1) and (2.2) are transformed from the physical domain into the computational

domain by

$$\tau = t, \quad \xi = x, \quad \psi = y, \quad \zeta = \frac{z - \eta(x, y, t)}{h - \eta(x, y, t)} h, \quad (\text{A1a-d})$$

where ξ, ψ, ζ and τ are respectively the space and time coordinates in the computational domain, and $h = L_z$ is the mean domain height. The Jacobian matrix corresponding to the transformation (A 1) is

$$J = \begin{bmatrix} \frac{\partial \xi}{\partial x} & \frac{\partial \xi}{\partial y} & \frac{\partial \xi}{\partial z} \\ \frac{\partial \psi}{\partial x} & \frac{\partial \psi}{\partial y} & \frac{\partial \psi}{\partial z} \\ \frac{\partial \zeta}{\partial x} & \frac{\partial \zeta}{\partial y} & \frac{\partial \zeta}{\partial z} \end{bmatrix} = \begin{bmatrix} 1 & 0 & 0 \\ 0 & 1 & 0 \\ \frac{\zeta - h}{h - \eta} \frac{\partial \eta}{\partial x} & \frac{\zeta - h}{h - \eta} \frac{\partial \eta}{\partial y} & \frac{h}{h - \eta} \end{bmatrix}. \quad (\text{A2})$$

Then the governing equations (2.1) and (2.2) become

$$J_{ji} \frac{\partial u_i}{\partial \xi_j} = 0, \quad (\text{A3})$$

$$\begin{aligned} \frac{\partial u_i}{\partial \tau} + \delta_{j3} \frac{\partial \zeta}{\partial t} \frac{\partial u_i}{\partial \xi_j} + J_{kj} \frac{\partial (u_i u_j)}{\partial \xi_k} &= - \frac{J_{ji}}{\rho} \frac{\partial p}{\partial \xi_j} + J_{kj} \frac{\partial \tau_{ij}^d}{\partial \xi_k} \\ &+ \nu J_{nj} \frac{\partial}{\partial \xi_n} \left(J_{kj} \frac{\partial u_i}{\partial \xi_k} \right) + B(t) \delta_{i1}, \end{aligned} \quad (\text{A4})$$

where the time derivative in the physical space is calculated by

$$\frac{\partial}{\partial t} = \frac{\partial}{\partial \tau} + \frac{\zeta - h}{h - \eta} \frac{\partial \eta}{\partial t}. \quad (\text{A5})$$

In the above equation, the pressure p is calculated at each time step by solving the Poisson equation, while $B(t)$ is prescribed by (2.3). The wave surface boundary conditions are provided by the Airy wave solution (Dean & Dalrymple 1991)

$$\eta(x, t) = a \cos(kx - \omega t), \quad (\text{A6})$$

$$u_s(x, t) = \omega a \cos(kx - \omega t), \quad (\text{A7})$$

$$w_s(x, t) = \omega a \sin(kx - \omega t), \quad (\text{A8})$$

where u_s and w_s are the horizontal and vertical orbital velocities at the wave surface, respectively, and a is the wave amplitude. The angular frequency ω and the wavenumber k satisfy the dispersion relation for deep water $\omega^2 = gk$.

Appendix B. Normalized mean wind velocity defect

We examine the initial evolution of the mean profile in the near surface region by using a different scaling of the velocity. Following He & Seddighi (2013), we define

$$\hat{U}(\zeta, t) = \frac{U(\zeta, t) - U(\zeta, 0)}{U(L_z, t) - U(L_z, 0)}, \quad (\text{B1})$$

where $U(L_z, t)$ is the mean velocity at the top boundary of the computational domain. The results are plotted in figure 22. The temporal evolution of the (velocity) boundary

Gusty wind turbulence over a travelling wave

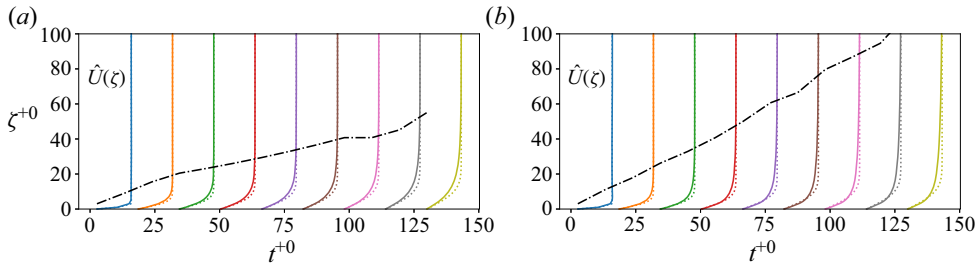


Figure 22. Evolution of the normalized mean wind velocity profiles $\hat{U}(\zeta, t)$ defined in (B1) in (a) the growing wind and (b) the decaying wind, in case CU8. The velocity profiles are plotted during $2.65 < t^{+0} < 130$, and the time interval between two consecutive velocity profiles is $\Delta t^{+0} = 15.9$. Our numerical result and the Stokes problem solution are denoted by the solid lines and dashed lines, respectively. Also plotted is the boundary layer thickness δ_{99} , denoted by the black dash-dotted line.

layer thickness δ_{99} is similar to a boundary layer developing in space. When the wind gust starts ($t \approx 0$), this normalized velocity is constant, i.e. $\hat{U}(\zeta > 0) = 1$, except at the surface, i.e. $\hat{U}(\zeta = 0) = 0$. For laminar flows over a flat plate, the mean profile then yields the solution to the Stokes problem: $\hat{U}(\zeta, t) = \text{erf}(\zeta)/\sqrt{\nu t}$, where erf is the error function. For the present flow over a travelling wave, the distribution of $\hat{U}(\zeta, t)$ is also similar to the Stokes solution (figure 22) because the viscosity dominates this high-shear region. However, the deviation of the LES result from the Stokes solution is slightly larger than that in a transient channel flow (He & Seddighi 2015) because of the wave geometry and wave orbital velocity.

Appendix C. Critical layer at steady state

The critical layer, at which height the mean wind speed equals the wave phase velocity, corresponds to a singular point in the inviscid Rayleigh equation and thus plays a significant role in the Miles (1957) wave-growth mechanism. In case CU8, the critical layer at $t = 0$ is close to the surface (figure 3), in the buffer layer, owing to the small wave age. In case CU42, ζ_c is larger than the computational domain height (not plotted). At such a height $\zeta > O(\lambda)$, the wave-coherent motions are much weaker than the turbulence motions (Sullivan & McWilliams 2010). Therefore, the critical layers in both case CU8 and case CU42 have little dynamic effects on wave growth. On the other hand, in case CU19, ζ_c is sufficiently large that the critical layer is in the logarithmic region, but not too large so that the wave-coherent motions can still be identified at this height. In figure 23, we plot the phase-averaged velocity at the steady state in the wave-following frame for case CU19 to illustrate the qualitative feature of the critical layer. As shown, across the critical layer height ζ_c , there is a change in the sign of $\langle u \rangle - c$, resulting in the closed loops of the streamlines. This phenomenon, also known as the cat-eye structure (Lighthill 1962), is consistent with the observations in previous studies (e.g. Sullivan *et al.* 2000; Yang & Shen 2010).

Appendix D. Calculation of form drag

Here, we outline the calculation of the form drag in (3.12) and (3.13). Following (2.6), we can rewrite the wave-coherent pressure at the wave surface as

$$\tilde{p}(x, \zeta = 0) = \text{Re}[\tilde{p}](\zeta = 0) \cos(kx) - \text{Im}[\tilde{p}](\zeta = 0) \sin(kx). \quad (\text{D1})$$

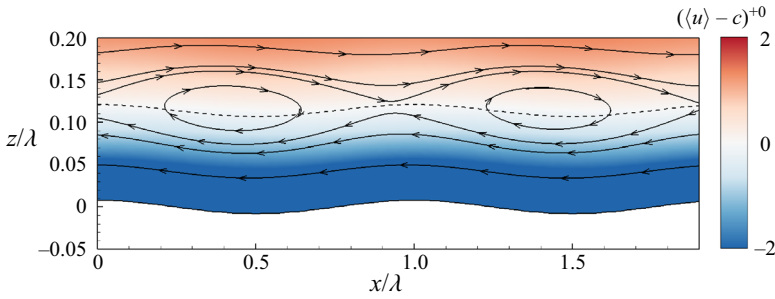


Figure 23. Streamlines of the phase-averaged velocity in the moving frame of reference in case CU19 for growing wind at $t = 0$. The streamwise velocity magnitude is denoted by the contour colour. Also plotted is the critical layer height, denoted by the black dashed line.

In the moving frame, the surface elevation is fixed, $\eta(x) = a \cos(kx)$, where a is the wave amplitude, thus $\eta_x(x) = -ka \sin(kx)$. Substituting this into the definition of the form drag and noting that only the wave-coherent part of pressure can contribute to wave growth, we can obtain

$$\tau_p = \frac{1}{L_x} \int_0^{L_x} p \eta_x dx = \frac{ka}{L_x} \int_0^{L_x} (\text{Im}[\tilde{p}] \sin^2(kx) - \text{Re}[\tilde{p}] \sin(kx) \cos(kx)) dx. \quad (\text{D2})$$

Note that the integral of the second part is zero. Therefore, the calculation of the form drag is simplified to

$$\tau_p = ka \text{Im}[\tilde{p}]|_{\zeta=0}. \quad (\text{D3})$$

The information of $\text{Im}[\tilde{p}]$ is connected to \tilde{w} by taking the imaginary part of the wave-coherent momentum equation (3.4) and rearranging the terms:

$$\frac{1}{\rho} \frac{d \text{Im}[\tilde{p}]}{d\zeta} = -k(U - c) \text{Re}[\tilde{w}] - \frac{\partial \text{Im}[\tilde{w}]}{\partial t} + \text{Im}[\mathcal{T}] + \text{Im}[\mathcal{V}]. \quad (\text{D4})$$

The above equation can be integrated, and after neglecting the higher-order terms, we can obtain

$$\frac{\text{Im}[\tilde{p}]|_{\zeta=0}}{\rho} = \int_0^\lambda k(U - c) \text{Re}[\tilde{w}] d\zeta + \int_0^\lambda \frac{\partial \text{Im}[\tilde{w}]}{\partial t} d\zeta. \quad (\text{D5})$$

REFERENCES

ABDALLA, S. & CAVALERI, L. 2002 Effect of wind variability and variable air density on wave modeling. *J. Geophys. Res.* **107** (C7), 3080.
 ÅKERVIK, E. & VARTDAL, M. 2019 The role of wave kinematics in turbulent flow over waves. *J. Fluid Mech.* **880**, 890–915.
 ANNENKOV, S. Y. & SHRIRA, V. I. 2011 Evolution of wave turbulence under ‘gusty’ forcing. *Phys. Rev. Lett.* **107** (11), 114502.
 BELCHER, S. E. & HUNT, J. C. R. 1993 Turbulent shear flow over slowly moving waves. *J. Fluid Mech.* **251**, 109–148.
 BUCKLEY, M. P. & VERON, F. 2016 Structure of the airflow above surface waves. *J. Phys. Oceanogr.* **46** (5), 1377–1397.
 BUCKLEY, M. P., VERON, F. & YOUSEFI, K. 2020 Surface viscous stress over wind-driven waves with intermittent airflow separation. *J. Fluid Mech.* **905**, A31.

Gusty wind turbulence over a travelling wave

- CALHOUN, R.J., STREET, R.L. & KOSEFF, J.R. 2001 Turbulent flow over a wavy surface: stratified case. *J. Geophys. Res.* **106** (C5), 9295–9310.
- CAO, T., DENG, B.-Q. & SHEN, L. 2020 A simulation-based mechanistic study of turbulent wind blowing over opposing water waves. *J. Fluid Mech.* **901**, A27.
- CAO, T. & SHEN, L. 2021 A numerical and theoretical study of wind over fast-propagating water waves. *J. Fluid Mech.* **919**, A38.
- CHOI, H. & MOIN, P. 2012 Grid-point requirements for large eddy simulation: Chapman's estimates revisited. *Phys. Fluids* **24** (1), 011702.
- DEAN, R.G. & DALRYMPLE, R.A. 1991 *Water Wave Mechanics for Engineers and Scientists*. World Scientific.
- DONELAN, M.A., BABANIN, A.V., YOUNG, I.R. & BANNER, M.L. 2006 Wave-follower field measurements of the wind-input spectral function. Part II: parameterization of the wind input. *J. Phys. Oceanogr.* **36** (8), 1672–1689.
- DONELAN, M.A. & PIERSON, W.J. 1987 Radar scattering and equilibrium ranges in wind-generated waves with application to scatterometry. *J. Geophys. Res.* **92** (C5), 4971–5029.
- DRUZHININ, O.A., TROITSKAYA, Y.I. & ZILITINKEVICH, S.S. 2012 Direct numerical simulation of a turbulent wind over a wavy water surface. *J. Geophys. Res.* **117**, C00J05.
- ECMWF 2020 *IFS Documentation CY47R1 – Part VII: ECMWF Wave Model*. IFS Documentation, vol. 7. ECMWF.
- GEORGE, W.K. & HUSSEIN, H.J. 1991 Locally axisymmetric turbulence. *J. Fluid Mech.* **233**, 1–23.
- GERMANO, M., PIOMELLI, U., MOIN, P. & CABOT, W.H. 1991 A dynamic subgrid-scale eddy viscosity model. *Phys. Fluids A* **3** (7), 1760–1765.
- GIGLIO, D., GILLE, S.T., SUBRAMANIAN, A.C. & NGUYEN, S. 2017 The role of wind gusts in upper ocean diurnal variability. *J. Geophys. Res.* **122** (9), 7751–7764.
- GRARE, L., PEIRSON, W.L., BRANGER, H., WALKER, J.W., GIOVANANGELI, J.-P. & MAKIN, V. 2013 Growth and dissipation of wind-forced, deep-water waves. *J. Fluid Mech.* **722**, 5–50.
- HAO, X., CAO, T. & SHEN, L. 2021 Mechanistic study of shoaling effect on momentum transfer between turbulent flow and traveling wave using large-eddy simulation. *Phys. Rev. Fluids* **6** (5), 054608.
- HAO, X. & SHEN, L. 2019 Wind-wave coupling study using LES of wind and phase-resolved simulation of nonlinear waves. *J. Fluid Mech.* **874**, 391–425.
- HARA, T. & SULLIVAN, P.P. 2015 Wavy boundary layer turbulence over surface waves in a strongly forced condition. *J. Phys. Oceanogr.* **45**, 868–883.
- HE, S. & JACKSON, J.D. 2000 A study of turbulence under conditions of transient flow in a pipe. *J. Fluid Mech.* **408**, 1–38.
- HE, S. & SEDDIGHI, M. 2013 Turbulence in transient channel flow. *J. Fluid Mech.* **715**, 60–102.
- HE, S. & SEDDIGHI, M. 2015 Transition of transient channel flow after a change in Reynolds number. *J. Fluid Mech.* **764**, 395–427.
- HENN, D.S. & SYKES, R.I. 1999 Large-eddy simulation of flow over wavy surfaces. *J. Fluid Mech.* **383**, 75–112.
- HRISTOV, T.S., MILLER, S.D. & FRIEHE, C.A. 2003 Dynamical coupling of wind and ocean waves through wave-induced air flow. *Nature* **422** (6927), 55–58.
- HUSAIN, N.T., HARA, T. & SULLIVAN, P.P. 2022a Wind turbulence over misaligned surface waves and air–sea momentum flux. Part I: waves following and opposing wind. *J. Phys. Oceanogr.* **52** (1), 119–139.
- HUSAIN, N.T., HARA, T. & SULLIVAN, P.P. 2022b Wind turbulence over misaligned surface waves and air–sea momentum flux. Part II: waves in oblique wind. *J. Phys. Oceanogr.* **52** (1), 141–159.
- HUSSAIN, A.K.M.F. & REYNOLDS, W.C. 1972 The mechanics of an organized wave in turbulent shear flow. Part 2. Experimental results. *J. Fluid Mech.* **54** (02), 241–261.
- HWANG, P.A., GARCÍA NAVA, H. & OCAMPO-TORRES, F.J. 2011 Observations of wind wave development in mixed seas and unsteady wind forcing. *J. Phys. Oceanogr.* **41** (12), 2343–2362.
- JANSSEN, P.A.E.M. 2004 *The Interaction of Ocean Waves and Wind*. Cambridge University Press.
- KIHARA, N., HANAZAKI, H., MIZUYA, T. & UEDA, H. 2007 Relationship between airflow at the critical height and momentum transfer to the traveling waves. *Phys. Fluids* **19** (1), 015102.
- KOMEN, G.J., CAVALERI, L., DONELAN, M.A., HASSELMANN, K., HASSELMANN, S. & JANSSEN, P.A.E.M. 1994 *Dynamics and Modelling of Ocean Waves*. Cambridge University Press
- LIBERZON, D. & SHERMER, L. 2011 Experimental study of the initial stages of wind waves' spatial evolution. *J. Fluid Mech.* **681**, 462–498.
- LIGHTHILL, M.J. 1962 Physical interpretation of the mathematical theory of wave generation by wind. *J. Fluid Mech.* **14** (3), 385–398.

- LILLY, D.K. 1992 A proposed modification of the Germano-subgrid-scale closure method. *Phys. Fluids A* **4** (3), 633–635.
- LOZANO-DURÁN, A., GIOMETTO, M.G., PARK, G.I. & MOIN, P. 2020 Non-equilibrium three-dimensional boundary layers at moderate Reynolds numbers. *J. Fluid Mech.* **883**, A20.
- MILES, J.W. 1957 On the generation of surface waves by shear flows. *J. Fluid Mech.* **3** (02), 185–204.
- MILES, J. & IERLEY, G. 1998 Surface-wave generation by gusty wind. *J. Fluid Mech.* **357**, 21–28.
- NIKOLAYEVA, Y.I. & TSIMRING, L.S. 1986 Kinetic model of the wind generation of waves by turbulent wind. *Izv. Atmos. Ocean. Phys.* **22**, 102–107.
- SMAGORINSKY, J. 1963 General circulation experiments with the primitive equations. *Mon. Weath. Rev.* **91** (3), 99–164.
- STEVENS, R.J.A.M. & MENEVEAU, C. 2017 Flow structure and turbulence in wind farms. *Annu. Rev. Fluid Mech.* **49** (1), 311–339.
- SULLIVAN, P.P., EDSON, J.B., HRISTOV, T. & MCWILLIAMS, J.C. 2008 Large-eddy simulations and observations of atmospheric marine boundary layers above nonequilibrium surface waves. *J. Atmos. Sci.* **65** (4), 1225–1245.
- SULLIVAN, P.P. & MCWILLIAMS, J.C. 2010 Dynamics of winds and currents coupled to surface waves. *Annu. Rev. Fluid Mech.* **42**, 19–42.
- SULLIVAN, P.P., MCWILLIAMS, J.C. & MOENG, C. 2000 Simulation of turbulent flow over idealized water waves. *J. Fluid Mech.* **404**, 47–85.
- SULLIVAN, P.P., MCWILLIAMS, J.C. & PATTON, E.G. 2014 Large-eddy simulation of marine atmospheric boundary layers above a spectrum of moving waves. *J. Atmos. Sci.* **71**, 4001–4027.
- TOBA, Y. 1972 Local balance in the air–sea boundary processes. *J. Oceanogr.* **28** (3), 109–120.
- WANG, L.-H., ZHANG, W.-Y., HAO, X., HUANG, W.-X., SHEN, L., XU, C.-X. & ZHANG, Z. 2020 Surface wave effects on energy transfer in overlying turbulent flow. *J. Fluid Mech.* **893**, A21.
- WASEDA, T., TOBA, Y. & TULIN, M.P. 2001 Adjustment of wind waves to sudden changes of wind speed. *J. Oceanogr.* **57** (5), 519–533.
- WORLD METEOROLOGICAL ORGANIZATION (WMO) 2018 *Guide to Instruments and Methods of Observation: Volume I – Measurement of Meteorological Variables*, 2018th edn.
- XUAN, A., DENG, B.-Q. & SHEN, L. 2020 Numerical study of effect of wave phase on Reynolds stresses and turbulent kinetic energy in Langmuir turbulence. *J. Fluid Mech.* **904**, A17.
- YANG, Z., DENG, B.-Q. & SHEN, L. 2018 Direct numerical simulation of wind turbulence over breaking waves. *J. Fluid Mech.* **850**, 120–155.
- YANG, D., MENEVEAU, C. & SHEN, L. 2013 Dynamic modelling of sea-surface roughness for large-eddy simulation of wind over ocean wavefield. *J. Fluid Mech.* **726**, 62–99.
- YANG, D. & SHEN, L. 2010 Direct-simulation-based study of turbulent flow over various waving boundaries. *J. Fluid Mech.* **650**, 131–180.
- YANG, D. & SHEN, L. 2011a Simulation of viscous flows with undulatory boundaries. Part I: basic solver. *J. Comput. Phys.* **230** (14), 5488–5509.
- YANG, D. & SHEN, L. 2011b Simulation of viscous flows with undulatory boundaries. Part II. Coupling with other solvers for two-fluid computations. *J. Comput. Phys.* **230** (14), 5510–5531.
- YOUSEFI, K., VERON, F. & BUCKLEY, M.P. 2020 Momentum flux measurements in the airflow over wind-generated surface waves. *J. Fluid Mech.* **895**, A15.
- YOUSEFI, K., VERON, F. & BUCKLEY, M.P. 2021 Turbulent and wave kinetic energy budgets in the airflow over wind-generated surface waves. *J. Fluid Mech.* **920**, A33.
- ZAVADSKY, A. & SHEMER, L. 2012 Characterization of turbulent airflow over evolving water-waves in a wind-wave tank. *J. Geophys. Res.* **117** (6), C00J19.
- ZAVADSKY, A. & SHEMER, L. 2017 Water waves excited by near-impulsive wind forcing. *J. Fluid Mech.* **828**, 459–495.
- ZENG, X., ZHANG, Q., JOHNSON, D. & TAO, W.-K. 2002 Parameterization of wind gustiness for the computation of ocean surface fluxes at different spatial scales. *Mon. Weath. Rev.* **130** (8), 2125–2133.